Available on CMS information server **CMS NOTE 2005/025**

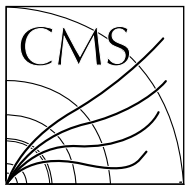

The Compact Muon Solenoid Experiment

CMS Note

Mailing address: CMS CERN, CH-1211 GENEVA 23, Switzerland

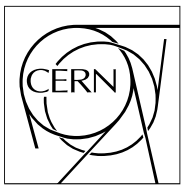

December 21st, 2005

Design and Test Beam Performance of Substructures of the CMS Tracker End Caps

R. Brauer[9], K. Klein[9], W. Adam[1], R. Adolphi[9], M. Ageron[6], S. Assouak[5], B. Atz[12], T. Barvich[12], W. Beaumont[2], F. Beissel[10], T. Bergauer[1], J.D. Berst[8], R. Blaes[7], M. Bleyl[11], P. Blum[12], F. Boegelspacher[12], W. de Boer[12], K.-D. Boffin[10], J.-L. Bonnet[5], O. Bouhali[3], W. Braunschweig[9], J.M. Brom[8], G. Bruno[5], E. Chabanat[6], F. Charles[7], B. Clerbaux[3], D. Contardo[6], B. De-Callatay[5], J. De-Favereau-de-Jeneret[5], C. Delaere[5], S. De-Visscher[5], J.-P. Dewulf[3], J. D'Hondt[4], F. Didierjean[8], G. Dirkes[12], F. Drouhin[7], M. Duda[10], J.P. Ernenwein[7], H. Esser[9], N. Estre[6], M. Fahrer[12], D. Favart[5], L. Feld[9], J. Fernandez[12], A. Flossdorf[10], G. Flugge[10], J.C. Fontaine[7], T. Franke[10], K. Freudenreich[13], M. Frey[12], M. Friedl[1], R. Fruehwirth[1], A. Furgeri[12], U. Goerlach[8], R. Goorens[4], G. Gregoire[5], E. Grigoriev[12], L. Gross[8], K. Hangarter[10], R. Haroutunian[6], F. Hartmann[12], B. Hegner[10], S. Heier[12], A. Heister[9], Th. Hermanns[10], J. Heyninck[4], U. Holm[11], J. Hrubec[1], P. Juillot[8], W. Karpinski[9], S. Kasselmann[10], Th. Keutgen[5], R. Klanner[11], S. König[9], M. Krammer[1], Th. Kress[10], C. Kukulies[9], E. de Langhe[2], G. Leibenguth[5], V. Lemaitre[5], G. de Lentdecker[3], A. Linn[10], A. Lounis[8], S. Lowette[4], N. Lumb[6], W. Lustermann[13], C. Maazouzi[8], D. Michotte[5], O. Militaru[5], L. Mirabito[6], J. Mnich[10], T. Muller[12], L. Neuckermans[3], A. Ninane[5], A. Nowack[10], C. Olivetto[8], J. Olzem[9], T. Ortega-Gomez[12], A. Ostaptchouk[9], S. Ovyn[5], D. Pandoulas[9], F. Pauss[13], U. Pein[11], M. Pernicka[1], S. Perries[6], G. Pierschel[9], K. Piotrzkowski[5], M. Poettgens[10], O. Pooth[10], F. Raupach[9], B. Reinhold[10], V. Roberfroid[5], X. Rouby[5], S. Schael[9], P. Schleper[11], N. Schirm[11], A. Schultz von Dratzig[9], G. Schwering[9], R. Siedling[9], H.-J. Simonis[12], P. Steck[12], G. Steinbrück[11], M. Stoye[11], R. Strub[8], M. Tasevsky[2], S. Tavernier[4], S. Tesch[11], A. Theel[12], M. Thomas[9], B. Trocme[6], O. Van-der-Aa[5], M. Vander-Donckt[5], C. Vander-Velde[3], P. Vanhove[8], P. Vanlaer[3], L. Van Lancker[4], R. van Staa[11], D. Vintache[8], W. Waltenberger[1], T. Weiler[12], K. Wick[11], J. Wickens[3], M. Wlochal[9], E. de Wolf[2], C. Yu[4], V. Zhukov[12]

[1] Institut f¨ur Hochenergiephysik derÖsterreichischen Akademie der Wissenschaften, HEPHY, Vienna, Austria

[2] Universiteit Antwerpen, Antwerpen, Belgium

[3] Université Libre de Bruxelles, Brussels, Belgium

[4] Vrije Universiteit Brussel, Brussels, Belgium

[5] Université Catholique de Louvain, Louvain-la-Neuve, Belgium

[6] Institut de Physique Nucléaire de Lyon, Université Claude Bernard Lyon-1, Lyon, France

[7] Université de Haute Alsace, Mulhouse, France

[8] Institut de Recherches Subatomiques, Strasbourg, France

[9] I. Physikalisches Institut, RWTH, Aachen, Germany

[10] III. Physikalisches Institut, RWTH, Aachen, Germany

[11] Institute for Experimental Physics, University of Hamburg, Hamburg, Germany

[12] Institut fur Experimentelle Kernphysik, Universit¨at Karlsruhe, Karlsruhe , Germany

[13] Eidgen¨ossische Technische Hochschule, IPP-LHP, Z¨urich, Switzerland

Abstract

With its total active silicon area of about 200 m^2 and more than 15000 silicon modules the silicon strip tracker of the CMS experiment at the LHC will be the largest silicon strip detector ever built. While the performance of single silicon modules has already been tested extensively in various test beam experiments, the performance of larger integrated substructures also had to be studied with a particle beam before launching mass production, in order to ensure the envisaged performance of the overall system. In May/June 2004 the performance of a system of two petals of the tracker end caps (TEC), which represents about 1% of the full TEC and forms an autonomous unit in terms of data acquisition, has been studied in a test beam experiment at CERN. In this document the test beam experiment is described and results are presented.

1 Introduction

With more than 15000 silicon modules, adding up to a total active silicon area of about $200\,\mathrm{m}^2$ and roughly 10 million electronics channels, the CMS silicon strip tracker will be the largest silicon detector ever built. The total detector will have a length of 5.4 m and a diameter of 2.4 m and will cover a region in pseudorapidity of up to 2.5. It will be located in a support tube and cooled to an operating temperature of below $-10\,^\circ\mathrm{C}$.
While single silicon modules have already been studied extensively within CMS since a long time, the performance of larger subsystems of the tracker has been studied only recently in system tests and in test beam experiments. In May/June 2004 the performance of a system of two petals of the tracker end caps (TEC), which represents about 1% of the full TEC and forms an autonomous unit in terms of data acquisition, has been studied in a test beam experiment at CERN. In this document the test beam experiment is described. The performance of the TEC petals during the test beam is discussed and results are presented.
The structure of this document is as follows: in Section 2 the general layout of the CMS silicon strip tracker is introduced and the readout and control architecture is explained. The layout of the TEC petals, both in terms of mechanics and electronics, is outlined in Section 3. The test beam experiment is described in Section 4. In Section 5 the analysis method is explained and the results are presented. Finally the main results are summarized in Section 6.

2 The CMS Silicon Strip Tracker

2.1 Layout of the CMS Silicon Strip Tracker

The active components of the silicon strip tracker are the silicon modules. Each module consists of four main parts: a support frame made of carbon fiber and/or graphite, a Kapton strip which delivers the bias voltage to the sensor back plane and insulates the sensor from the frame, the hybrid with the front-end electronics, and one or two silicon sensors, depending on the module type. The sensors are single-sided microstrip detectors with AC-coupled p-type strips in an n-type bulk. Modules mounted within a radial distance of 60 cm from the beam line have 320 µm thick sensors, while the sensors of modules with a larger radial distance have a thickness of 500 µm. More than 20 different module geometries exist, with rectangular and wedge shaped sensors and strip pitches ranging from 80 µm to 205 µm. Both single-sided and double-sided modules, the latter with two single-sided modules mounted back to back with a stereo angle of 100 mrad, are used[1)]. Details about the sensor design can be found in Ref. [1].
The CMS silicon strip tracker is divided into four subsystems: the Tracker Inner Barrel (TIB), the Tracker Inner Disks (TID), the Tracker Outer Barrel (TOB) and the Tracker End Caps (TEC). The modularity of the system can be seen in Fig. 1, where a cross-section through one quarter of the detector is shown. While in the two barrel detectors the silicon strips are running parallel to the beam, the modules on the disks and in the end caps are arranged in rings such that the strips are running in the radial direction.
The TIB consists of four cylindrical layers. Each layer is constructed out of four carbon fiber (CF) half-shells (two half-shells on each z side[2)]). Strings carrying three thin modules are mounted inside and outside of the layer surfaces. The TID is composed out of three disks per side. On each disk the modules are arranged in three rings.
The TOB is constructed out of six cylindrical layers. The basic substructure of the TOB is a rod: a CF support frame, which carries either three double-sided (layers 1-2) or three single-sided (layers 3-6) thick modules on each side.
Finally, each of the two end caps of the TEC consists of nine carbon fiber disks. The basic substructure of the TEC is a petal, a wedge shaped carbon fiber support plate which carries up to 28 wedge shaped modules arranged in up to seven radial rings. On each disk 16 petals are mounted, namely eight front and eight back petals, which are of slightly different geometry and carry different numbers of modules.
A detailed description of the layout of the silicon strip tracker is available in Refs. [2] and [3].

2.2 Readout and Control Architecture

Figure 2 shows a schematic and simplified view of the readout and control architecture used in the CMS silicon strip tracker. The signals of the 512 or 768 silicon strips of a module are processed by four or six APV25 readout

[1)] In the following, the term "module" is used for single-sided modules, i.e. also for each of the two sub-modules of a double-sided module. If double-sided modules, consisting of two single-sided modules, are referred to, the term "double-sided module" is used explicitly.

[2)] In the CMS coordinate system the x-axis points towards the centre of the LHC ring, the y-axis points upwards and the z-axis completes the right-handed coordinate system. The azimuthal angle in the xy-plane is denoted as ϕ.

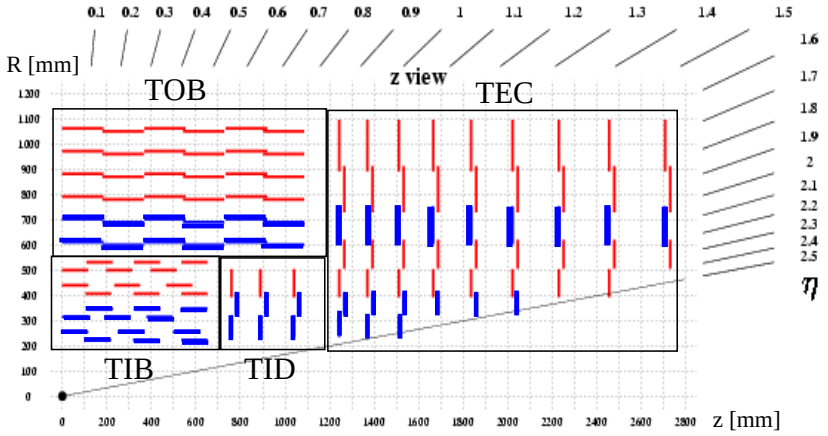

Figure 1: The CMS silicon strip tracker. A cross-section of one quarter of the detector is shown in the longitudinal view. The thin red and thick blue lines represent single-sided and double-sided silicon modules, respectively.

chips [4] that are mounted on the front-end hybrid (FE-hybrid) [5]. The APV25 is built in radiation hard 0.25 μm CMOS technology. It is a 128 channel chip which samples at a frequency of 40 MHz and implements a charge-sensitive amplifier with a time constant of 50 ns, a shaper and a 192 cell pipeline that provides a 3.2 μs trigger latency. After arrival of a first level trigger the signals are processed by an analogue circuit, for which two operation modes can be chosen: in peak mode only one data sample is used, while in deconvolution mode three consecutive data samples are reweighted and summed up [6]. In this way the original impulse signal is recovered, which leads to a much shorter pulse and thus to correct bunch crossing identification in the high luminosity running phase of the LHC. The signals of two chips are multiplexed onto one data line by the APVMUX chip. The analogue electrical signals are then transmitted differentially over a distance of a few centimetres to opto-electrical converter devices (Analogue Opto-Hybrids or AOHs), consisting basically of laser drivers [7], which modulate the drive currents of edge-emitting laser diodes [8]. The data are then transmitted to the counting room via single-mode fibres over a distance of about 100 m. In the counting room 96 channel VMEbus readout boards called Front End Drivers or FEDs [9] will be housed. The FEDs will be equipped with optical receivers and will provide digitization and

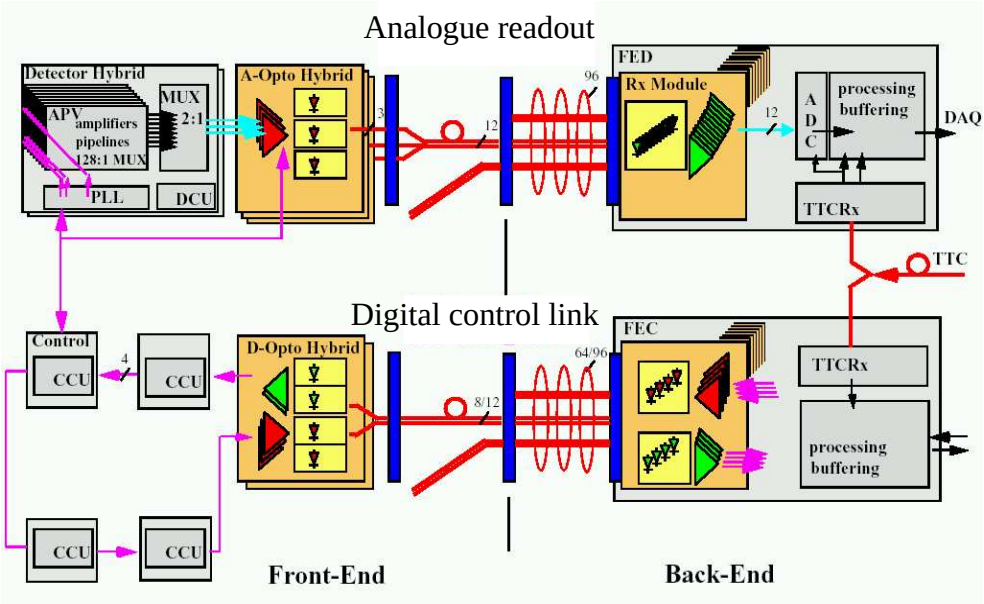

Figure 2: Schematic and simplified view of the readout and control architecture of the CMS silicon strip tracker. Only one front-end hybrid with its connections to the analogue readout (FED) and to the digital control link (FEC) is shown.

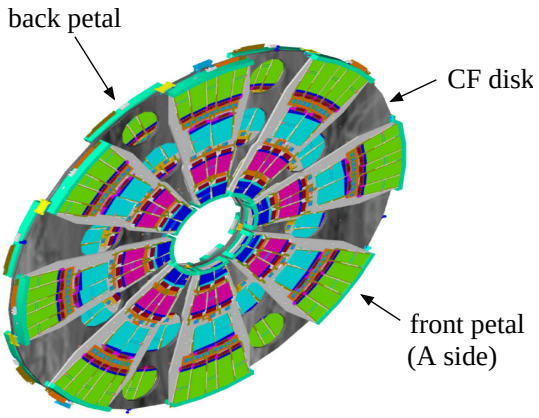

Figure 3: Technical drawing of one disk of the tracker end cap, with the interaction region to the right. In this drawing, eight front and eight back petals are mounted. Only the "A side" of the front petals, with rings 1, 3, 5 and 7, is visible.

(optionally) first processing (e.g. pedestal subtraction and cluster finding) of the data. In a local memory the data are stored until requested by higher levels of the data acquisition.
Controlling of the electronics will be handled by VMEbus cards called Front End Controllers or FEC cards, which will also be located in the counting room. The FECs distribute the LHC clock and the first level trigger signals received from the global LHC Timing Trigger and Command (TTC) system [10]. Timing as well as control signals are transmitted to the detector via a digital optical link [11]. On the petal, rod or shell, the conversion of optical to electrical signals and vice versa is carried out by dedicated opto-electrical converter devices, the digital opto-hybrids (DOHs) [11]. The electrical signals are then encoded by dedicated chips called Communication and Control Units (CCU25) [12], which are mounted on small PCBs, so-called CCU modules (CCUMs), located on the motherboard on the petal or rod structure. The CCU25 communicates with the FEC via a token ring protocol and distributes the timing signals to the Phase Locked Loop (PLL) chips [13], which are located on the front-end hybrid of each module, while the control signals are distributed via the I^2C protocol [14] to the addressed chips on the appropriate devices (modules, AOHs or DOHs).
An eight channel twelve bit ADC, the Detector Control Unit (DCU) [15], is implemented on the FE-hybrid, to allow for the monitoring of the leakage current, the low voltages on the hybrid and the temperatures of the silicon sensors, the hybrid and the DCU itself.

3 Design of TEC Petals

3.1 Mechanical Layout and Cooling

In the TEC the silicon modules are mounted onto wedge shaped carbon fiber support plates, so-called petals, to obtain a manageable modularity.
Petals come in two flavours: front petals (FPs) are a bit broader and carry up to 28 modules, back petals (BPs) carry up to 23 modules. On each carbon fiber disk, eight front petals are mounted on the side that faces the interaction region, while eight back petals are mounted in the ϕ gaps between the front petals on the other side of the disk. Back and front petals overlap slightly in ϕ. In Fig. 3 a technical drawing of one disk is shown.
The modules are arranged in seven radial rings on both sides of the petals. Both sides of a front and a back petal are shown in Figs. 4 and 5, respectively. Table 1 summarizes the number of modules per ring on each side for both petal types. When looking from the interaction region, the side A of the front petals is visible, while side B faces the disk. For the back petals, side C faces the disk, while side D points to the far end of the detector.
Due to the fact that a fixed pseudorapidity corresponds to larger radii for greater z, the inner rings are not present on all disks. As can be seen in Fig. 1, only disks 1-3 carry all seven rings, while on disks 4-6 ring 1 is missing, on disks 7 and 8 rings 1 and 2 are missing, and on disk 9 only rings 4-7 are present.
The modules of rings 1-4 consist of one 320 µm thick sensor each, while for the modules of the outer rings 5-7 two 500 µm thick sensors are bonded together.
To obtain tracking information in the radial direction, double-sided modules are used for rings 1, 2 and 5, consisting of a "normal" module (with the strips running in radial direction) and a "stereo" module each. The two modules are mounted back to back such that the strips of the stereo module are rotated by 100 mrad with respect

	Front petal		Back petal	
	Side A	Side B	Side C	Side D
Ring 1N	2	-	1	-
Ring 1S	2	-	1	-
Ring 2N	-	2	-	1
Ring 2S	-	2	-	1
Ring 3	3	-	2	-
Ring 4	-	4	-	3
Ring 5N	2	-	3	-
Ring 5S	2	-	3	-
Ring 6	-	4	-	3
Ring 7	5	-	5	-

Table 1: The number of modules per ring for both sides of front and back petals. Only the petals of disks 1-3 carry all rings. The abbreviations N and S stand for "normal" and "stereo" modules.

to the strips of the normal module. While single-sided TEC modules have sensors with 512 strips, all double-sided TEC modules have sensors with 768 strips and, consequently, are read out by six instead of four APVs.
To ensure full spatial coverage, neighbouring petals overlap in ϕ, neighbouring rings overlap in the radial direction, and also individual modules are mounted with an overlap in ϕ. "Mounting bridges" consisting of aluminium and CF provide the necessary support. The ϕ overlap of modules as well as the mounting bridges are clearly visible in Figs. 4 and 5.
The electronics on the hybrid has to be cooled to avoid overheating, and after irradiation the silicon sensors have to be cooled as well to suppress reverse annealing and to avoid thermal runaway due to the exponential temperature dependence of the leakage currents. Cooling is provided by a titanium cooling pipe of approximately 7 m length and an inner diameter of 3.9 mm, embedded inside the petal. Two individual 3.5 m long pipes are laser welded to a titanium manifold and in this way they are connected in series. In Fig. 6 the petal cooling circuit is shown.

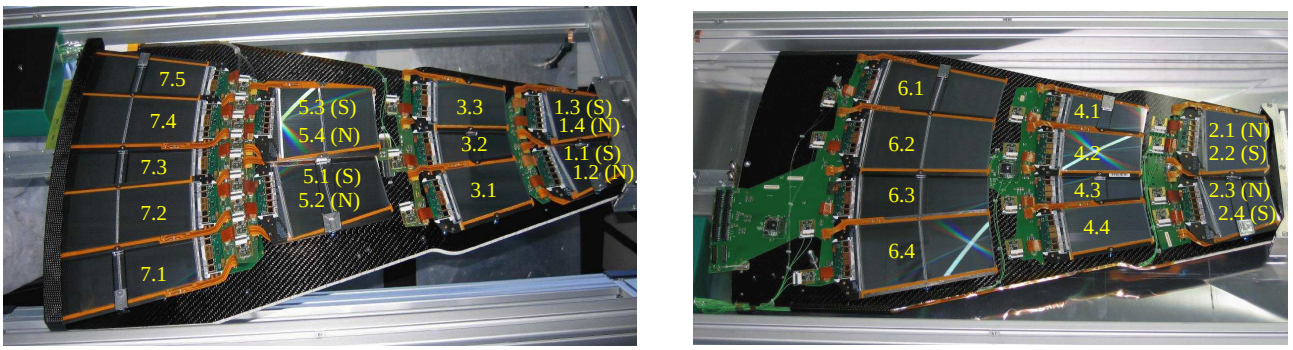

Figure 4: Side A (left) and side B (right) of a front petal. The numbering scheme of the silicon modules is shown.

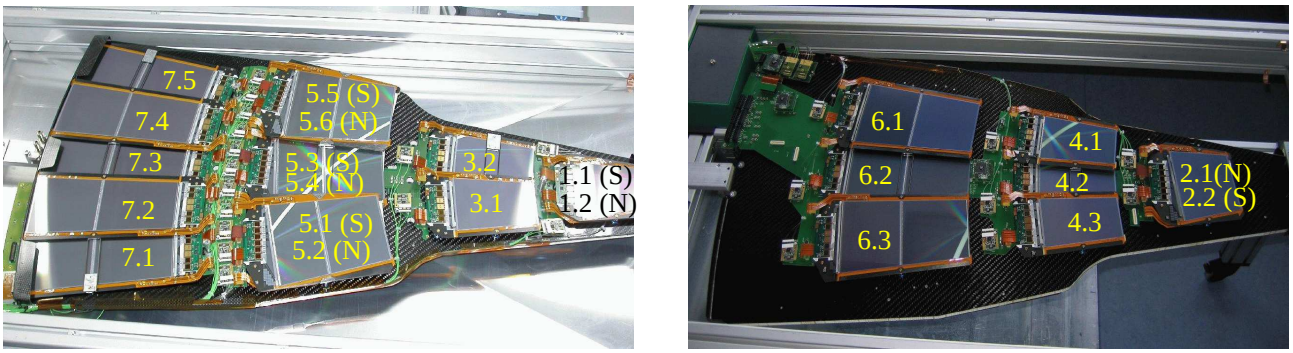

Figure 5: Side C (left) and side D (right) of a back petal. The numbering scheme of the silicon modules is shown.

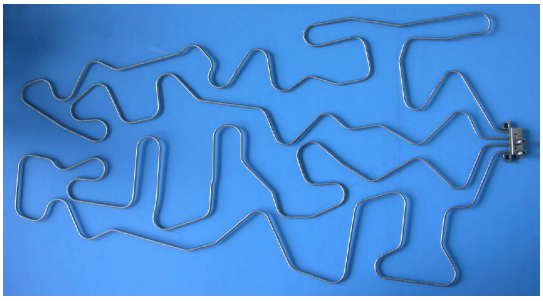

Figure 6: A cooling pipe that has already been laser welded to the cooling manifold (left), and a petal being glued inside the glueing jig (right).

The modules are mounted onto inserts, aluminium pieces that are glued directly onto the cooling pipe and provide both precision mechanical mounting and thermal contact between the module and the pipe. The analogue opto-hybrids are screwed onto inserts (one insert per AOH) as well. Each petal carries of the order of 100 cooling inserts. To glue the inserts precisely to the pipes, dedicated gluing jigs are used. In Fig. 6 such a jig with a petal inside is shown. Finally a relative precision of the positions of the threaded holes in those inserts of $5\,\mu$m in all three dimensions is achieved by means of precision milling.

3.2 The InterConnect Board

To bring power, timing and control signals to the electronic devices (modules, AOHs, CCUMs) on the petal, motherboards, called InterConnect Boards or ICBs, are mounted on both sides of the petal. In Fig. 7 photos of a bare front petal equipped only with ICBs are shown. There are five individual boards: the main board ICB_46 on side B, which carries all the connectors for the cables and the two CCUM boards and transmits power and signals to the modules of rings 4 and 6, and four smaller boards, which provide the power and signals for the other rings (ICB_2 on side B and ICB_1, ICB_3 and ICB_57 on side A, where the numbers correspond to the number of the ring to which the connected modules belong). These four boards are connected (for the boards on side A and D via holes in the petal) to the main board.
The following services and signals are provided and transmitted by the ICB:

- the low voltage, namely 2.50 V and 1.25 V for the module electronics and the AOHs,
- the supply voltage (2.5 V) for the CCUMs,
- high voltage (HV) to bias the silicon modules (up to 500 V),
- LVDS signals: the 40 MHz clock signal with encoded reset and trigger signals, and control data signals,
- PIA (Peripheral Interface Adapter) reset signals that are sent from the CCU to the devices on the petal,
- I^2C control signals for the steering of the parameter settings of the readout electronics and the optical converter electronics,
- monitoring signals from temperature and humidity sensors,
- analogue data transmission from the front-end hybrid to the AOH,
- the analogue and digital electrical ground.

For each module position, there are three connectors on the ICB: one for the front-end hybrid, one for the AOH, and one for the bias Kapton which is used to bring the HV-bias to the backplane of the modules and to read out the temperature probes located on the Kapton.
The design of the ICB is clearly a tradeoff between optimal performance and a material budget as low as possible. To keep the number of LV power supplies and connections relatively small on the one hand while limit the current that must be provided by one power supply on the other hand, the modules are organized in three low voltage (LV) groups, which will be served by individual power supplies (Tab. 2). In total there are eleven power rails on ICB_46, which must carry a current of up to 12 A, and, for material budget reasons, are rather narrow. Capacitances are implemented on the ICB near the power input connectors as well as near the front-end connectors to

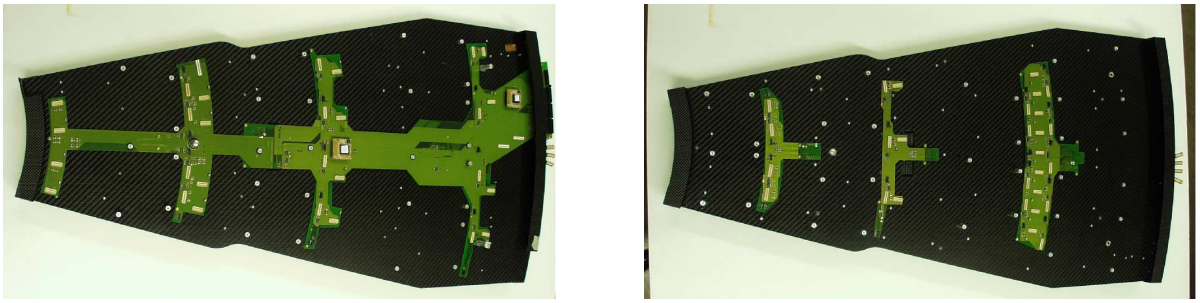

Figure 7: The different ICBs on the two sides of a front petal: ICB_2 and ICB_46 on side B, and ICB_1, ICB_3 and ICB_57 on side A (from left to right). On ICB_46, the two CCUMs are plugged.

suppress ripples and reduce the voltage overshoot on the power lines caused by switching off the FE-hybrids.
To carry all power rails and signal traces, the ICB_46 and ICB_57 have six copper layers, while the smaller boards have only four layers. To minimize the material budget, copper layers have been designed to be as thin as possible: 17 and 25 μm for the inner four and outer two layers, respectively. A cross sectional cut through the board ICB_46 can be seen in Fig. 8. Digital traces (L4 in Fig. 8) are shielded by power and ground layers (L3, L5).
For each low voltage group, two high voltage channels are provided. For each HV channel there are up to four single HV lines, which power one or two silicon modules.
Sensing is implemented both for the low and high voltage connections. The sense resistors for the low voltage are located in the electrical centre of each power group.
The FEC and the CCUMs on the petal are connected in a token ring topology, where timing and control signals are transmitted from the FEC to the CCUMs via a LAN protocol with NRZI (Non-Return-to-Zero Inverted) decoding. Two petals, one back and one front, make up one control ring. The digital signals are transmitted optically to the petal and back to the FEC. On the petal the Digital Opto-Hybrids take care of the conversion of the optical signals to electrical LVDS signals and vice versa. Two DOHs are located on a PCB, the Digital Opto-Hybrid Module (DOHM), which is mounted on the back petal. From the DOHM, which also distributes the power for the DOHs, signals are transmitted to the CCUMs on the petal. The front petal is the first in the control loop. From the CCUMs, the timing signals (trigger and reset are encoded in the clock signal) are transmitted to the PLL chips on the hybrids.
The control signals are converted to I^2C signals by the CCU and are sent to the appropriate chips. In each I^2C clock line, a 470 Ω resistor is implemented to limit the current drawn from the CCU. Since this resistor leads to longer transition times for the clock signals, which in turn can lead to problems with the I^2C communication, 2.2 nF shunt capacitors are implemented in parallel to these resistors. It has been verified in the system test that this configuration leads to stable I^2C communication.
Analogue data from the FE hybrid are transmitted differentially to the AOH over short distances (a few centimetres). Data traces are shielded by one ground and one power layer.
Low-pass filters are implemented for both temperature and HV traces to ensure that noise is not coupled in via these lines.
In the test beam, the latest prototypes of the ICBs have been used. In the final version, available since mid 2004, there is one difference with respect to this prototype. For technical reasons (solderability) the copper layer closest to the detector has been made thicker (35 μm) on boards ICB_1, ICB_3 and ICB_57 on the front petal and ICB_1, ICB_2 and ICB_3 on the back petal (the other boards are produced by a different company). To leave the material budget basically invariant, this layer has been fabricated as a mesh instead of a solid layer. It has been verified in the system test that no significant changes in the noise behaviour have been introduced by this change.

LV group	Rings	Number of modules (FP / BP)	Number of APVs (FP / BP)
Group 1	1, 2	8 / 4	48 / 24
Group 2	3, 4, 6	11 / 8	44 / 32
Group 3	5, 7	9 / 11	44 / 56

Table 2: Organisation of rings in low voltage groups, and number of modules and APVs per group. The first and second numbers are for front and back petals (of disks 1-3), respectively.

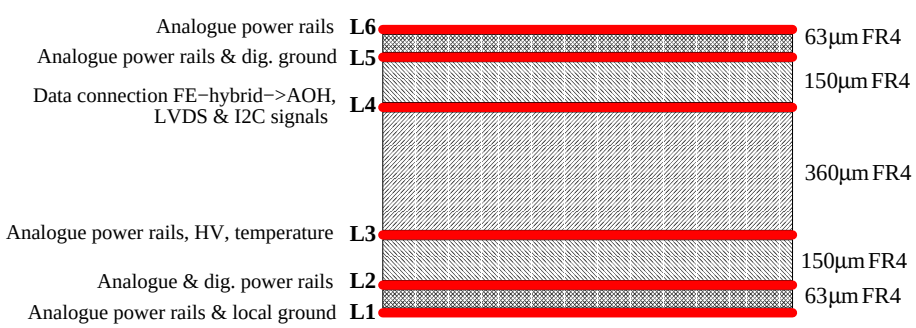

Figure 8: The layer structure of the ICB_46 (not to scale).

3.3 The Grounding Scheme

The so-called TEC common ground will be located at the back end of each TEC. It will be realized by means of a 5 cm wide and 150 µm thick copper ring, which will be glued to the outer radius of each back disk[3)] and tied to the brackets that connect the tracker support tube to the hadron calorimeter. The material of the hadron calorimeter represents a perfect solid ground. The shields of all cables, the reference points of all power groups, the cooling manifolds that are used to connect the cooling pipes of the petals to the main tubes that are mounted on the TEC, the CF skins of the disks and petals and the outer aluminium shields of the TEC will be connected to this TEC common ground.

The grounding of a control loop is shown schematically in Fig. 9. On the petal side, one common analogue ground is implemented per petal. This so-called local petal ground is distributed via a 2 cm wide and 20 µm thick copper path along the ICBs as a reference rail. The LV and HV supplies of all power groups are referenced to this local petal ground at the geometrical/electrical centre of each group. The digital ground of a control group is referenced once to the local petal ground. The local petal ground of each petal will be connected to the TEC common ground. Copper strips glued to the outer radii of the disks and along the service channels that connect all disks with the back disk provide the electrical connection to the TEC common ground. These copper strips are connected via short copper braids to the ICBs on the petals.

The carbon frames of the silicon detectors are insulated electrically from the cooling pipes and connected via a conductive glue spot to the bias Kapton and finally via the ICB to the FE hybrid ground. Electrical insulation of modules with respect to the cooling pipe is provided by an anodized layer between the cooling inserts and the cooling pipe.

In CMS, all LV and HV power supplies will be floating.

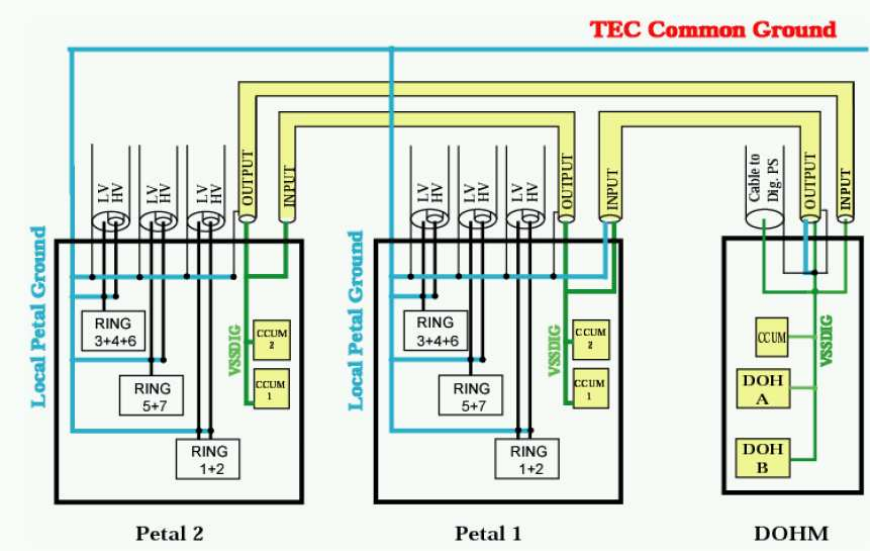

Figure 9: Schematic view of the grounding scheme of a control loop.

3) The back disk is a tenth disk that carries alignment components.

4 The Test Beam Experiment (May/June 2004)

4.1 Test Beam Area and Beam Conditions

From May 27th until June 21st a test beam experiment was performed at the CERN West area. Protons from the SPS [16] are used to produce a secondary or tertiary beam consisting either of muons with a momentum between 70 GeV and 120 GeV, or pions with a momentum of 120 GeV (with a small muon contamination). The beam is steered to the test beam area called X5. From June 14th onwards an LHC-like beam was provided. In this operation mode, particles are delivered in 2-3 ns long bunches spaced by 25 ns. A total of 48 bunches are provided per SPS revolution (23 μs) during the spill. The spill is the 2.2 s long period within a 12 s long SPS cycle, during which particles are delivered.

Two setups of the tracker were exposed to the beam. The beam first traversed a tracker outer barrel setup consisting of six rods fully equipped with modules, and then passed the TEC setup consisting of two petals. The trigger scintillator was located between the TOB and the TEC setup.

Typical primary trigger rates were 2000 muons per spill and 600000 pions per spill. This corresponds to mean occupancies of 15 Hz/cm^2 for muons and 70 kHz/cm^2 for pions during the spill. While the pion beam is rather focused, with an RMS of roughly 2 cm, the muons are widely spread and the beam profile is therefore determined by the size of the trigger scintillator. The beam profiles of the muon and pion beams can be seen in Fig. 10 and 11, respectively (the detailed definition of a cluster is given later in Sect. 5.1.2). The pion beam is therefore optimal for study of local high occupancy, while the muon beam is preferred for the study of global module parameters such as the signal-to-noise ratio.

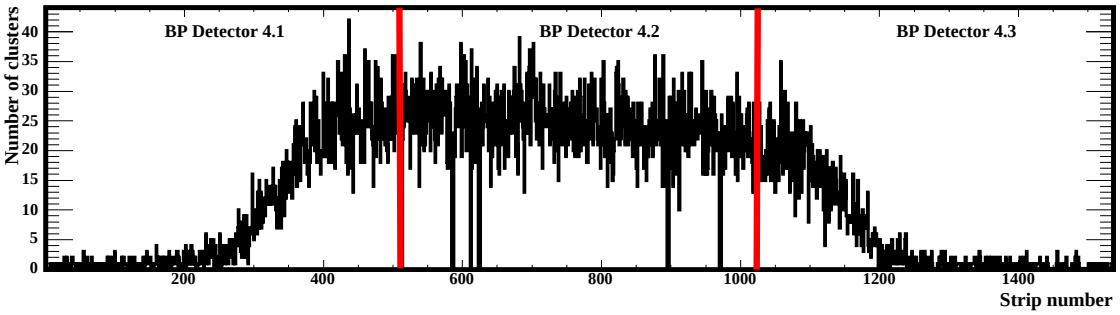

Figure 10: Profile of the muon beam, as seen on ring 4 on the back petal. The beam spreads out over all three modules of ring 4. For illustration, the profiles of the three modules are plotted next to each other, ignoring the ϕ overlap between the silicon sensors. The boundaries between the three modules are indicated by the two thick red lines. The holes in the profile are due to bad strips present on the modules.

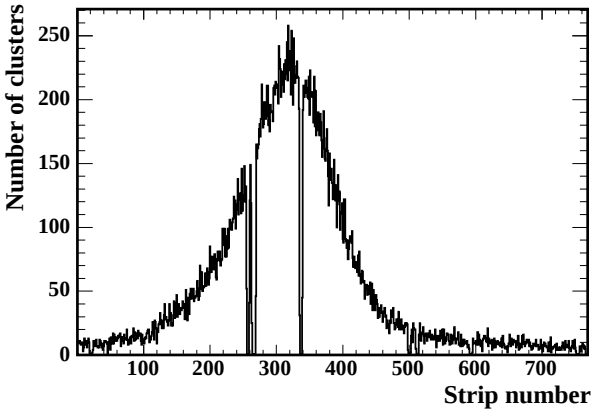

Figure 11: Profile of the pion beam, as seen on module 5.1 of the front petal. The holes in the profile are due to bad strips present on the module.

4.2 The Data Acquisition System

In the test beam the official tracker data acquisition (DAQ) software was used. This software is based on the XDAQ [17] framework. XDAQ is a middleware designed specifically for the development of distributed data acquisition systems within CMS, providing platform independent services, tools for local and remote inter-process communication, as well as technology-independent data storage.
The CMS DAQ system consists basically of the following elements: first the data are digitized by the FEDs. Upon reception of a trigger signal, they pass the data to the readout unit, where data are buffered and passed on to the event builder. The builder unit receives data fragments of an event from the readout units and builds them into full event buffers. These full events are finally transferred to the filter unit, where the high-level trigger algorithms are executed. Many more details about the DAQ architecture can be found in [18].
The test beam was performed with the most recent version of the DAQ software, based on XDAQ 2.0. The software was running under the Linux operating system on standard PCs. The different DAQ processes were distributed between five ports on four different PCs. Communication between the different processes is realized via the I2O (Intelligent Input/Output) protocol. A Java user interface (xdaqWin) served as run control. System configuration was done in a convenient way via XML files. Important system parameters could be changed also in the xdaqWin user interface. A JAS (Java Analysis Studio) [19] based online monitoring programm provided immediate feedback on the performance of all modules. Data were stored in compressed ROOT [20] files.
The readout rate was about 200 events per spill, to be compared with much higher trigger rates, as described in Sect. 4.1. The reason for the low performance was the slow data compression within ROOT. In the final experiment, the higher level DAQ part (including the event builder, filter, monitoring, online analysis) will be more efficient and much more distributed than in the test beam, to cope with the expected first level trigger rate of 100 kHz and a high level trigger rate of 100 Hz.

4.3 The TEC Setup

A full TEC control loop was operated and read out during the beam test. As mentioned in Sect. 3.2, a control loop consists of one front and one back petal. Both petals were fully equipped with modules, thus 51 modules corresponding to 124 optical readout channels had to be handled by the data acquisition. Corresponding to about 1 % of the final TEC, this was the largest tracker subsystem operated so far.
Mechanically, both petals were fixed inside rectangular aluminium profiles that are intended for transport and handling of petals during the mass production phase. The two frames were mounted inside a thermally insulated aluminium box that provided a cold and dark environment during operation. In Fig. 12 a photo of the box with the two petals is shown. The box was placed on an xy-table, which was movable such that the whole petal could be scanned with the particle beam. It must be stressed that the mechanical fixation of the petals was not precise and both the exact location of the petals with respect to each other and their orientation with respect to the beam axis are unknown. Therefore the possibility to study efficiency, tracking etc. is limited.
Since the CMS tracker volume will be cooled to a temperature of below $-10°$C and flushed with nitrogen at a temperature of $-20°$C, the TEC setup was operated in a cold and dry environment. The petals were connected in series to a 500 W cooling plant developed within CMS for test stands. The chiller was running with the fluid C_8F_{18} instead of the one that will be used in CMS (C_6F_{14}), since it is much easier to handle due to the higher boiling temperature (101°C vs. 56°C at a pressure of 1 atm [21]). To prevent condensation on the cold surfaces, the box was

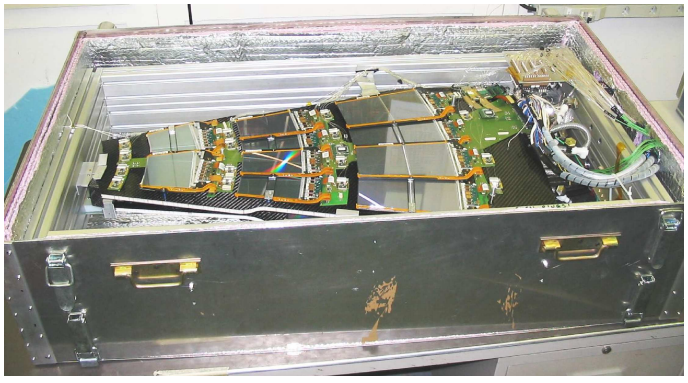

Figure 12: The two petals mounted in the insulated dark box.

flushed with dry nitrogen. The back flow of the cooling liquid was used to cool the nitrogen in a heat exchanger. Furthermore, a large copper plate equipped with a copper pipe was cooled with a second commercial chiller. This plate was mounted inside the box to provide active cooling of the environment. Typical operation parameters are a cooling plant outlet temperature of $-25°$C, a petal inlet temperature of $-20°$C, an air temperature of $-10°$C inside the box (the temperature on the sensors and FE-hybrids is discussed in Sect. 4.5.2) and a relative humidity of 3-4%. The temperature of the nitrogen blown into the box has not been measured.
Petals with anodized cooling inserts were not yet available for the test beam. The electrical insulation between the module frames and the cooling pipe was therefore realized by Kapton washers placed between the frame and the inserts. Kapton washers were also used to insulate the screws used for the module assembly from the module frames.
All electronics was located in the readout barrack roughly 10 m from the beam area.
The low voltage was provided by six floating laboratory power supplies that were developed within CMS for test stands. Two floating ISEG EHQ series power supplies provided the bias voltage. The connection between the power supplies and the petals was realized by 20-40 m long copper multiservice cables [22] [4)]. A simple floating laboratory power supply was used to power the control ring.
The control ring was fully optical. An optical PMC FEC was used, which consists of the final opto-electrical conversion device (mezzanine FEC) plugged onto a commercial PMC-to-PCI adapter card. Later in CMS eight of these mezzanine FECs will be mounted onto one 9U VME board (one mezzanine FEC per control ring). The DOHM, a close-to-final prototype, was equipped with two DOHs. Digital information was transmitted using prototypes of the 96 channel multi-ribbon cables that will be used in CMS.
For the first time in a test beam, a prototype of the final readout card, the VME-based FED, was used. It provides 96 readout channels, so two of these cards had to be operated within one VME crate, and one FED was used per petal.
Data were transported to the FEDs via optical ribbons: the AOH fibers were connected to 12-fiber ribbons, which were in turn connected to 96-fiber optical cables. On the readout barrack side, the cables were spliced into 12-fiber ribbons that could be plugged into the optical connectors on the FEDs.

4.4 Interlock and Slow Control

A prototype of the final tracker slow control and interlock system was used [18]. About 25 thermistors from Fenwal and three relative humidity sensors of type HIH3605B from Honeywell, distributed inside the box, were read out continuously and the values were displayed. From this information, the dew point was calculated. A PLC (Programmable Logic Controller) of the final type (Simatic S7-300 by Siemens) was used for the interlock of the low voltage power supplies and the cooling plant. The power supplies were interlocked when certain conditions (such as a fast rising temperature or temperature below the dew point) were met.
In addition to these external temperature probes, the thermistors on each module could be read out using the eight-channel ADC called the Detector Control Unit (DCU) that is located on the hybrid. On each module there are three thermistors: one on the bias Kapton below the back plane measuring the silicon temperature, one on the hybrid and one directly inside each DCU. Online monitoring of these temperatures was implemented and the data were stored in ROOT files.

4.5 Experiences from Operation of a TEC Control Loop

The beam test provided an excellent opportunity to gain experience in the operation of a large subsystem of the tracker in terms of system commissioning, operation and performance.

4.5.1 System Commissioning and Operation

Before useful data can be taken, the system has to be commissioned to assure correct timing settings and optimal utilisation of the dynamic range of the FEDs. The following steps were taken:

a.) The FED sampling time was chosen such that the amplitude of the digital signal had settled.

[4)] In the meantime it was decided to use a different type of cables, so-called Low Impedance Cables (LIC), for the connection from the power supplies to the patch panels at each end of the tracker support tube (bulkheads). Aluminium multi-service cables will still be used for the connection from the bulkheads to the petals or rods.

b.) The sampling of all readout channels was synchronized (details about the synchronization procedure can be found in [23]). According to the position of a module on the petal or rod, different trigger transmission times are observed. In addition, the analogue data are transmitted via optical fibers, ribbons and multi-ribbon cables that are not necessarily of the same length for different modules. This leads to different data transmission times between the detectors and the FED, for which corrections are required. The adjustment was made via PLLs on the hybrid and inside the FED on a per-module basis.

c.) Each event is stored in the APV pipeline for up to 3.2 μs until a trigger signal is received. The trigger signal travels from the scintillator to the FEC, where it is processed and passed to the detector. The PLL encodes the trigger signal and sends it to the APV after an adjustable delay. First this delay was adjusted in steps of 25 ns (the length of a pipeline cell) to ensure that the correct pipeline cell was read out. Once the correct cell was found, a finer adjustment (in steps of 1.04 ns) of the trigger latency was performed to sample on the maximum of the signal pulse. Only in this way it can be assured that the optimal signal is recorded. These adjustments of the coarse and fine delay within the PLL were common for all modules (since in step b.) corrections for the variations between different modules have already been made).

d.) Care was taken to ensure that the optical chain responded linearly to the signals of the APV. The AOH gain and bias current and the APV baseline were chosen such that signals corresponding to 3.2 minimal ionising particles (MIPs) for thin and 2 MIPs for thick detectors were still within the linear range. This adjustment was done on a per-fiber basis, and, since the response of the laser diodes is temperature sensitive, it was also done separately for each operating temperature.

In practise, special types of "runs" are implemented in the DAQ software, e.g. a run type for the adjustment of the sampling point, run types for the tuning of the trigger latency (both for coarse and fine tunings of the trigger delay), and a run type for the tuning of the optical parameters (gain and bias). The output of these runs was provided to the operator as text output in the shell and had to be inserted by hand into the XML files which contain the system parameter settings. The commissioning procedures had been developed for laboratory readout systems consisting of a few modules, and it was the first time that a large system comprising 124 readout channels had to be commissioned. Taking into account the complexity of the system and the large number of channels, the commissioning worked remarkably well. First useful data could be taken after about two days. On the other hand it became obvious that without automation the commissioning is time and manpower intensive and that the system is too sensitive to operator errors. Work on an automation of the procedures was started due to this experience, and in a further test beam experiment in September 2004 a much higher level of automation was already provided.
Once the system had been commissioned, actual system operation was very convenient. The DAQ was usually running stably over time periods of the order of 1 hour and the user interface was flexible and easy to use.

4.5.2 System Stability and Hardware Performance

The performance of the TEC petals was in general very satisfying.
The system was running stably from the beginning. The I^2C communication was reliable both in cold and warm operation, with the exception of a few positions where electronics components relevant to the I^2C communication were missing on the ICB or were equipped incorrectly [5)].
The grounding scheme was very similar to the final one: the local petal grounds of the two petals were connected externally, and the two digital grounds via the control ring copper cables. The digital ground of the front petal was tied to the local petal ground via a jumper on the ICB_46. Stable operation was observed when the local petal ground was connected to the "X5 ground" (a solid grounded metal bar), which can be regarded as the equivalent of the TEC common ground mentioned in Sect. 3.3.
Out of the 51 modules in operation, a few exhibited problems, some of which were known before the test beam (one module had a broken readout channel, one a HV short, three showed a large common mode under certain conditions). Those problems were not system-related and are therefore not further discussed.
The system has been operated at room temperature during the first two days. After this time it was cooled to the minimal possible operating temperature whenever possible (warming-up was necessary a few times for technical reasons such as a leak in the heat exchanger). Typical hybrid operating temperatures were $+10\,°C$ and $0\,°C$ for hybrids with six and four APVs, respectively. The typical corresponding sensor temperatures are $-10\,°C$ and $-13\,°C$.

[5)] These mistakes happened mainly because several small design modifications related to the I^2C bus as explained in Sect. 3.2 were implemented shortly before the test beam and partly had to be added by hand to the ICBs used. It was determined only during and after the test beam that some components were wrongly equipped or missing, and thus there was inadequate time to correct these problems.

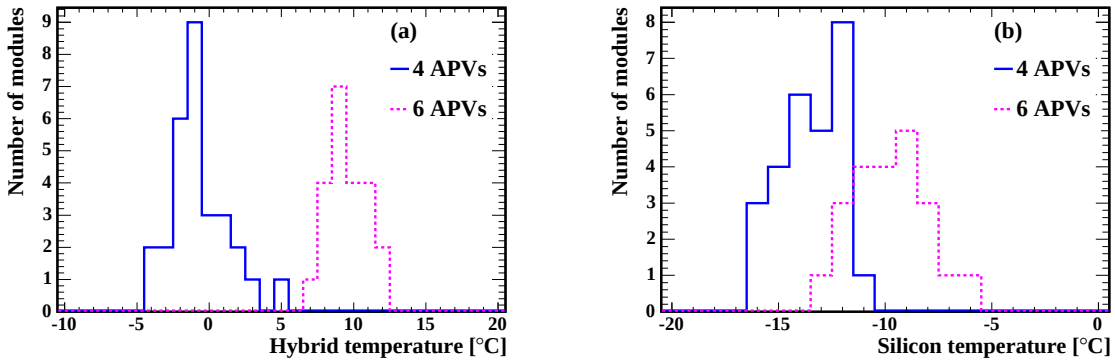

Figure 13: Typical operating temperatures of (a) hybrids and (b) silicon sensors for modules with six APVs (dashed line) and four APVs (solid line) during cooling.

The temperature distributions of all modules, measured via the DCU, are shown in Fig. 13. The petals have thus been operated at temperatures comparable to the operating temperatures expected in the final tracker.
However, it must be stressed that conditions were not realistic enough (unirradiated sensors were used, the temperature of the nitrogen was not known, Kapton washers were used to insulate the modules against the cooling pipe, etc.) to interpret the measurements as a quantitative test of the petal cooling system.

5 Test Beam Results

5.1 Analysis Method

5.1.1 General Characteristics of Silicon Strip Modules

In this chapter the definitions of the characteristical variables describing the properties of silicon strip modules are given.

The pedestal

The pedestal p_i of a strip i corresponds to the mean data output of this channel in absence of a physical signal. It is calculated from M events according to the formula:

$$p_i = \frac{1}{M}\sum_{j=1}^{M} r_{ij}\,,$$

where r_{ij} is the raw data value of strip i in event j.

The raw noise

The total or raw noise σ_i of strip i describes the fluctuation of its raw data output about the pedestal:

$$\sigma_i = RMS(r_{ij}) = \sqrt{\frac{1}{M}\sum_{j=1}^{M}\left(r_{ij}-p_i\right)^2}\,.$$

The raw noise is composed of an irreducible component, arising from the intrinsic noise of the detector and the electronics, and the common mode.

The common mode

The common mode describes a common deviation of several channels about the pedestal. It is calculated per event, and usually (and throughout this note) per APV chip (128 channels). The common mode CM_j of event j can be determined either from the mean

$$CM_j = \frac{1}{128}\sum_{i=1}^{128}(r_{ij}-p_i)$$

or the median of the deviation. The median is less sensitive to the tails of the distribution, and is therefore used in this ananlysis.

The common mode noise

The common mode noise is the RMS of the common mode distribution.

The common mode subtracted noise

The common mode can be subtracted event-wise from the raw data. The RMS of the resulting data is called the common mode subtracted noise σ^{CMS}:

$$\sigma_i^{CMS} = RMS(r_{ij} - CM_j) = \sqrt{\frac{1}{M}\sum_{j=1}^{M}(r_{ij} - CM_j - p_i)^2}\,.$$

The signal and signal-to-noise ratio

For calculation of the most probable value (MPV) of the signal and the signal-to-noise ratio (S/N), a Landau distribution convoluted with a Gaussian is fitted to the data. The most probable value of this distribution is quoted as the Signal S or S/N.

Definition of a cluster

A cluster can be composed of several strips: the seed strip, which has the highest signal-to-noise ratio, and the neighbour strips. A seed strip is required to have a signal-to-noise ratio greater than three, a neighbour strip is assigned to the cluster if its signal-to-noise ratio is greater than two, and the signal-to-noise ratio of the total cluster must be above five.
The noise on the strips is added in quadrature to obtain the cluster noise.

The equivalent noise charge

The noise in ADC counts depends on the gain of the readout chain and thus a direct comparison of different readout channels is impossible. Therefore, the noise is usually expressed as the number of electrons to which it corresponds, i.e. the equivalent noise charge, or ENC for short. For the normalization it is assumed that a MIP creates most likely 24000 electrons in 300 μm of silicon [3], and the beam particles are treated as MIPs. By comparing the most probable value (MPV) of the signal with the expected number of electrons, taking into account the effective thickness of the sensor, the conversion factor between ADC counts and electrons is calculated per APV.

5.1.2 Test Beam Analysis

In the following, the analysis of the test beam data is described on a more technical level.
For the offline analysis of the recorded data, an analysis package was developed [24]. In the framework of this package, raw data files can be processed. The code provides methods for calculation of pedestals, noise, common mode, flagging of bad strips and cluster finding. In the following, some details of the analysis such as the most important cuts are listed:

- The noise is calculated iteratively. In each iteration, the same data sample is processed in two passes: in the first pass pedestals and noise are calculated, in the second pass the common mode and noise after common mode subtraction are computed. From the second iteration onwards, clusters are identified based on the pedestals and noise from the previous iteration, and then pedestals and noise are computed with the pruned sample.
  - In the first iteration, raw noise and noise after CM subtraction are computed from 500 events. The pedestals and noise still contain a contamination from particle signals. Bad strips are identified based on the noise after CM subtraction. In runs with high local hit rates, strips might be wrongly identified as bad strips, since in this iteration clusters cannot be disregarded for noise computations.
  - In the second iteration pedestals and noise are recalculated from 500 events. The mask of bad strips is cleared and recomputed based on the noise after CM subtraction.

  - In the third iteration pedestals and noise are recalculated from 500 events. The mask of bad strips is updated.
  - In the last iteration, pedestals and noise are recalculated using 1000 events and the mask of bad strips is updated. If pedestals and noise are computed from a physics run, these 1000 events are taken from the middle of the run. If pedestals and noise are computed from a dedicated pedestal run, the last 1000 events of the pedestal run are used.

- The median of the ADC counts after pedestal subtraction, calculated per event and APV, is taken as the common mode.

- The common mode noise is determined by a Gaussian fit to the common mode noise distribution.

- Bad strips are identified based on the mean and RMS of the noise per APV. For the computation of the mean and RMS of the noise, the five strips with the highest and lowest noise, respectively, are disregarded (truncated mean).
  The number of bad strips was determined from the analysis of three run types [6)]:

  - pedestal runs in peak mode:
    * a strip is flagged as noisy if its noise exceeds the truncated mean noise of the APV by more than five times the RMS of the APV's noise;
    * a strip is flagged as dead if its noise is lower than the truncated mean noise of the APV minus five times the RMS of the APV's noise;
  - pedestal runs in deconvolution mode, using the same cuts as for runs in peak mode,
  - dedicated calibration runs, where a defined amount of charge is injected into the preamplifier using the internal calibration logic of the APV. In such runs strips were identified as bad using the following cuts:
    * a strip is considered to have a pin hole, if its pulse height is lower than 0.2 times the mean pulse height of all strips of the APV;
    * a strip is believed to have a short with one of its neighbours if it is not a pin hole, but its pulse height is lower than 0.8 times the mean pulse height of all strips of the APV;
    * a strip is considered to have an open bond if its pulse height exceeds the mean pulse height of all strips of the APV by 7 % and its rise time is at least 7 % lower than the mean rise time of all strips of the APV.

  Strips have been counted as bad, if they were flagged as bad in at least two out of these three run types.

- For cluster finding, the pedestals, noise after common mode subtraction and mask of bad strips from the fourth iteration are used.

- Clusters including a bad strip or located directly next to a bad strip are ignored.

- For the test beam data, in general the noise is calculated directly from the physics runs. The only exceptions are runs where a pion beam with an LHC-like time structure was used (details of the beam structure are explained in Sect. 4.1). In this case the noise is calculated from pedestal runs that have been taken shortly before a physics run. In pedestal runs an internal trigger is used, thus clusters are present only accidentally.

- For S/N distributions of whole modules only one-strip clusters are used, since otherwise the S/N depends e.g. on the angle to the beam and thus different modules are not directly comparable. For S/N distributions of single APVs, all clusters are used to ensure sufficient beam statistics.

All cuts are chosen such that they are as close as possible to the cuts used in the official CMS reconstruction software (ORCA) [25]. Using a sample of the data, it has been verified that the software used in this work produces results consistent with the results obtained by the official ORCA based software.

[6)] These cut values have empirically been found to provide good distinguishing power. However, no systematic optimization of the cut values has been performed.

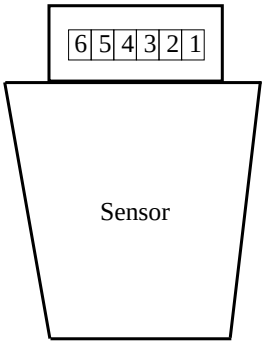

Figure 14: Numbering scheme for the APV chips on a module.

5.2 Results

With 51 modules in the beam, distributions can only be shown for a subset of modules. In Figs. 30-43 the most important characteristic distributions are shown for one module per ring and petal. These distributions are discussed in the following.
The numbering of the silicon modules on the petals is indicated in Figs. 4 and 5.

5.2.1 Pedestal Distributions

Pedestal distributions are shown in Figs. 30-43 (a). Typically the pedestal height is in the range of 200-350 ADC counts. The increase of the pedestal height with the strip number within one APV is a typical behaviour of the CMS silicon modules, and is believed to come from a drop of the supply voltage over the 128 channels of an APV, due to the finite resistance of the metal tracks that carry the supply voltage [26]. This gradient in the pedestal height does not affect adversely the performance of the modules.

5.2.2 Noise Performance

In Figs. 30-43 (b) the distributions of the raw and common mode subtracted noise both in peak and deconvolution mode are shown. These noise distributions were measured in the cold environment.
The noise performance observed in the test beam is satisfactory for all modules. As can be seen from the example distributions shown, only a small common mode is observed. In addition, all 51 modules exhibit flat noise corresponding to a flat common mode. During operation of the CMS tracker, the FED will be operated in zero suppression mode, and an online common mode subtraction with a flat common mode will be performed. The presence of a non-flat common mode, i.e. a common mode depending on the strip number, would thus lead to fake clusters.
The corresponding common mode distributions of the modules' first APV (the numbering scheme for the APVs on a module is depicted in Fig. 14) in peak mode are shown in Figs. 30-43 (c). The mean common mode noise, calculated from all working APVs of all modules, is (0.81 ± 0.31) ADC counts in peak mode and (0.95 ± 0.29) ADC counts in deconvolution mode. The mean of the common mode is compatible with zero within about one standard deviation: (0.001 ± 0.064) and (0.09 ± 0.07) ADC counts. The relatively large deviation from zero is due to the fact that the median algorithm was used to calculate the common mode.
On average the common mode subtracted noise in deconvolution mode is a factor of (1.36 ± 0.20) higher than in peak mode. This result corresponds reasonably well to the theoretical expectation of 1.63 based on measurements with single APV25 chips [3].

5.2.3 Number of bad Strips

The number of bad strips has been calculated for all modules using the algorithm described in Sect. 5.1.2.
In Fig. 15 (a) the distribution of the number of bad strips per module for all 51 modules is shown. On the back petal, 54 bad strips have been found, corresponding to 0.38 %, while on the front petal there were 75 bad strips, corresponding to 0.43 %. One dead readout channel on module 5.3 of the back petal is not included in these numbers. Considering that most modules have been used extensively in the system tests for a period of several months prior to the test beam, and that no specific selection of modules has been made, the module quality is excellent. In the official module qualification, modules with less than 2 % of dead strips are accepted.

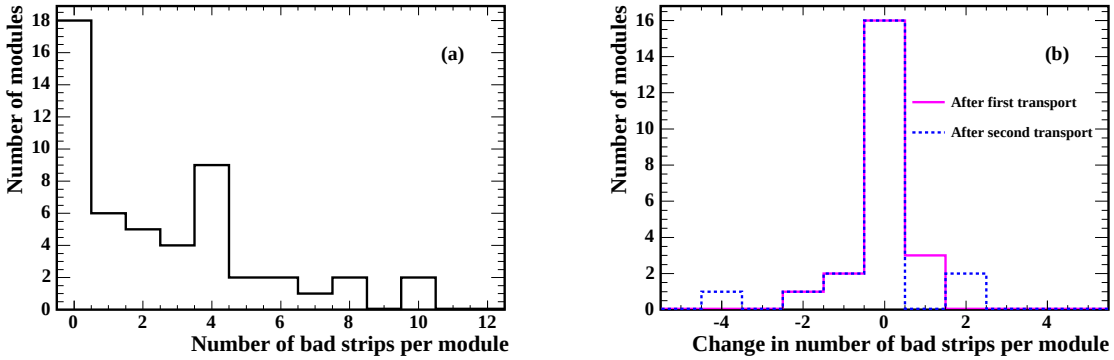

Figure 15: (a) Distribution of the number of bad strips per module for all 51 modules during the test beam, (b) change in the number of identified bad strips per module on the back petal after the transport to CERN (solid line) and back to Aachen (dashed line).

The back petal has been transported to CERN by car over a distance of roughly 800 km. To investigate possible damage due to this transport, the number of bad strips of the back petal has been determined three times[7]:

1. in Aachen before the test beam: 52 bad strips.
2. during the test beam: 51 bad strips;
3. in Aachen after the test beam: 47 bad strips.

Fig. 15 (b) shows the change in the number of bad strips per module for the two transports. Within the uncertainty of the analysis method [8], no strip was lost.

5.2.4 Signal and Signal-to-Noise Ratio

Peak mode signal distributions for the individual optical channels are shown in Figs. 30-43 (d) [9]. Even after a channel-by-channel optimization of the gain of the readout chain, as described in Sect. 4.5.1, a variation in the gain of the optical channels of one module is observed for several modules, as visible e.g. in Fig. 32 (d). The S/N, however, is not affected by this effect.
The most probable collected cluster charge in peak mode in the cold environment is shown in Fig. 16 for all available APVs. The mean from all APVs is (126 ± 17) ADC counts for 500 µm thick sensors and (77 ± 12) ADC counts for 320 µm thick sensors. Due to a different setting of the APV gain register, the signal in the final experiment will be about 15 % higher: approximately 145 ADC counts for thick sensors and 89 ADC counts for thin sensors, respectively. These numbers are roughly 12 % above the expectation of 129 (80) ADC counts for a minimum ionizing particle (MIP) traversing 500 µm (320 µm) of silicon, for optimized settings of the gain of the optical chain [27]. In the meantime the FED was modified to obtain a gain inside the specification.
The signal-to-noise distributions for the chosen subset of modules are shown in Figs. 30-43 (e) for both readout modes.
During the beam test, the S/N of almost all modules was measured under various conditions (in peak and deconvolution mode, in the warm and cold environment). In Fig. 17 the mean S/N per ring is plotted in peak and deconvolution mode for both operating temperatures. For the cold environment, in peak mode the S/N of thin modules is 27-33, while thick modules have a S/N of 35-42. In deconvolution mode the S/N is 19-22 and 20-24 for thin and thick sensors, respectively.

[7] After the test beam, one APV was broken, probably due to mishandling. This APV is taken out of the comparison, and therefore the numbers below do not correspond to the 54 bad strips quoted above for the test beam.

[8] Especially pin holes, i.e. shorts between the aluminium and the p+ implant due to a fault in the SiO_2 insulation layer, cannot always be identifi ed from their noise or calibration curves alone. In single module tests, dedicated pin holes tests are therefore performed using an LED light source to create charge in the detector. This test was not possible with the test beam setup.

[9] For some optical channels the statistics was insuffi cient, as can be seen from the height of the distributions, e.g. in Fig. 30 (d).

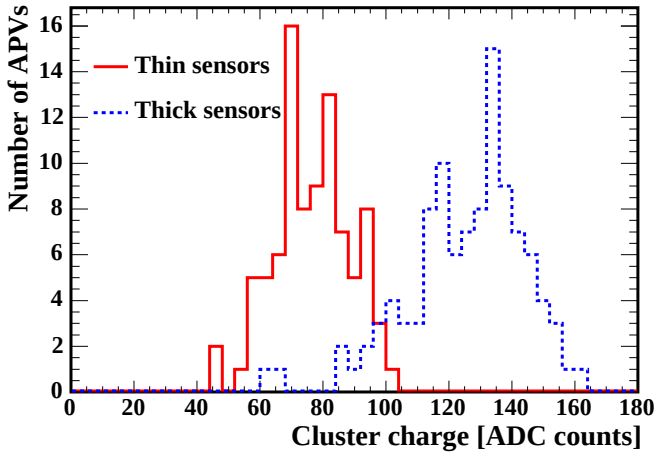

Figure 16: The mean cluster charge in peak mode for thin and thick sensors. All data were taken in the cold.

For a fixed sensor thickness, the remaining variation in S/N is caused mainly by the dependence of the noise on the module capacitance, which varies between the rings due to different strip lengths. Strip lengths [28] and sensor capacitances are listed in Table 3 for all rings. The capacitance was calculated from the length L, pitch p and strip width w using the formula

$$C_{\mathrm{tot}}\,[\mathrm{pF}] = \left(0.8\frac{\mathrm{pF}}{\mathrm{cm}} + 1.7\frac{w}{p}\frac{\mathrm{pF}}{\mathrm{cm}}\right) \cdot L\,[\mathrm{cm}]$$

with $\frac{w}{p} = 0.25$ [3]. The dependence of the noise on the capacitance will be discussed in more detail in the next section.
According to [29] a S/N of ten would still ensure a hit finding efficiency above 95% together with a low rate of fake hits. The high observed S/N therefore guarantees that a sufficiently high S/N will be measured even after ten years of operation in the hostile environment at the LHC, where a decrease of the S/N of about 25% is expected due to radiation damage effects [2].

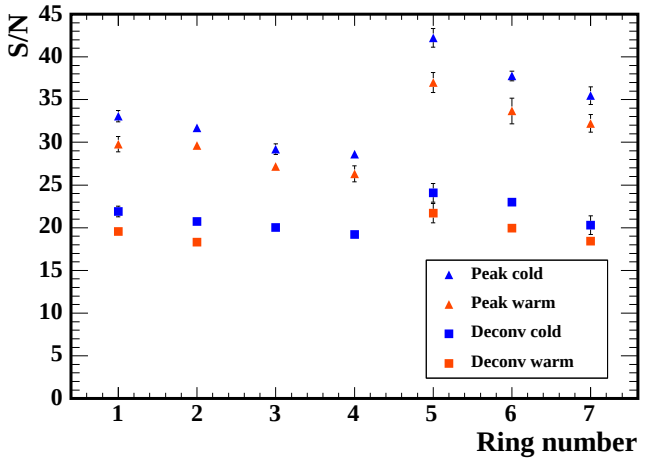

Figure 17: The mean signal-to-noise ratio per ring for peak and deconvolution mode and for the two operating temperatures. The error bars correspond to the RMS of the distribution of the S/N for a certain geometry. For rings 3 and 4, not enough data were taken in deconvolution mode at room temperature.

Ring number	Strip length [mm]	Capacitance [pF]
Ring 1	87.2	10.7
Ring 2	88.1	10.8
Ring 3	110.6	13.5
Ring 4	115.1	14.1
Ring 5	147.2	18.0
Ring 6	183.9	22.5
Ring 7	205.7	25.2

Table 3: Lengths of readout strips and sensor capacitances for modules of all rings.

5.2.5 Noise in Electrons

The ENC was calculated as described in Sect. 5.1 from the common mode subtracted noise distributions for each strip. The mean conversion factor calculated from all APVs is (311 ± 49) electrons / ADC count, where the uncertainty is the RMS of the resulting distribution of conversion factors for all APVs.
A few typical ENC distributions for peak mode are plotted in Figs. 30-43 (f). As expected, the steps between the readout channels present in some of the noise distributions of Figs. 30-43 (b) vanish.
Since the noise depends on the capacitance of the module and thus varies between rings, the mean ENC for each ring was calculated using all APVs with sufficient statistics. In Fig. 18 the mean noise per ring is plotted versus the strip length. As expected, a linear dependence is clearly observed. The measured ENC values can be compared with the expectation taking into account only the noise of the APV25 readout chip as measured in [30]:

$$\begin{aligned} \mathrm{ENC} &= 270\,e^- + 38\,e^-/\mathrm{pF}\cdot C \quad \text{for peak mode at room temperature;} \\ \mathrm{ENC} &= 430\,e^- + 61\,e^-/\mathrm{pF}\cdot C \quad \text{for deconvolution mode at room temperature.} \end{aligned}$$

As can be seen from Tab. 4, reasonable agreement is found, with the largest deviation amounting to 17 %. That the measured noise is mostly larger than the calculated noise can be understood from additional noise sources not included in the calculation, e.g. noise from the optical chain.
The mean common mode noise in electrons is shown in Fig. 19. It amounts to (173 ± 38) electrons in peak mode and (299 ± 76) electrons in deconvolution mode. The mean common mode is compatible with zero within about one standard deviation: (21 ± 17) electrons in peak mode and (-1 ± 21) electrons in deconvolution mode. The above numbers apply for the median algorithm. For the mean algorithm, the mean common mode is (4 ± 11) electrons in peak mode.
Based on the temperature behaviour of the MOSFET transistor as the basic building block of the APV25 readout chip, $N \propto \sqrt{T}$, and on measurements on APV25 chips, it is expected that the ENC in the cold environment is reduced by about 10-15 % with respect to room temperature, under the assumption of a temperature difference of the order of 40 °C [31]. Since the gain of the optical chain changes with temperature, this effect can only be

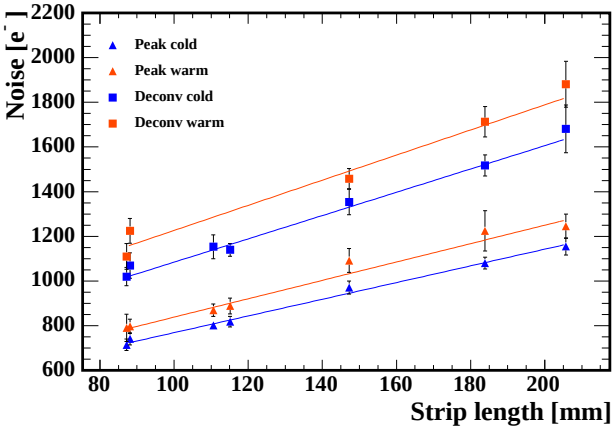

Figure 18: The mean ENC versus the strip length for peak and deconvolution mode and for the two operating temperatures. Each entry represents the mean ENC of a certain geometry, calculated from the means of all APVs with sufficient beam statistics. The uncertainties correspond to the RMS of the resulting distributions.

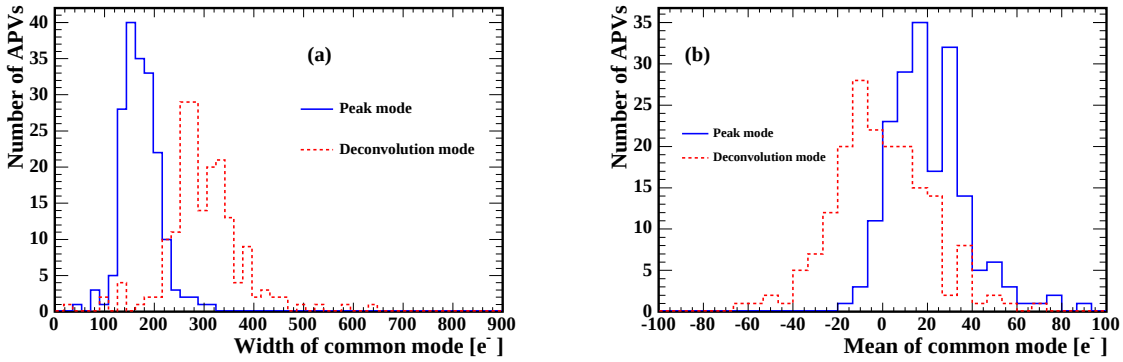

Figure 19: (a) Width and (b) mean of the common mode in peak (solid line) and deconvolution mode (dashed line), measured in the cold.

studied in the ENC. In Fig. 18 and Tabs. 4 and 5 the ENC of runs taken at room temperature and in the cold are compared. A reduction in ENC between 7 and 13 % with respect to the values obtained at room temperature is observed, in reasonable agreement with the expectation.
It can be regarded as a great success of the test beam that a full TEC control loop operated with the almost final readout chain and close to final grounding exhibits such a low noise, corresponding reasonably well to the theoretical expectation. The final power supplies used in CMS were not yet available for this measurement, but a test with prototypes of the final power supplies was performed shortly after the test beam. The common mode subtracted noise in ADC counts measured in this test was comparable to the one observed with the power supplies used during the test beam.

Ring number	Peak mode		Deconvolution mode	
	ENC measured [e$^-$]	ENC calculated [e$^-$]	ENC measured [e$^-$]	ENC calculated [e$^-$]
Ring 1	791 ± 61	677	1110 ± 57	1083
Ring 2	797 ± 32	680	1225 ± 55	1089
Ring 3	870 ± 28	783	no data available	1254
Ring 4	889 ± 36	806	no data available	1290
Ring 5	1092 ± 54	954	1458 ± 45	1528
Ring 6	1225 ± 90	1125	1712 ± 68	1803
Ring 7	1246 ± 54	1228	1881 ± 102	1967

Table 4: The measured and calculated ENC in peak and deconvolution mode for different module geometries, at room temperature. The uncertainty is the RMS of the resulting ENC distribution per geometry. For the calculation of the ENC, only the noise of the APV25 readout chip is taken into account.

Ring number	Peak mode	Deconvolution mode
	ENC measured [e$^-$]	ENC measured [e$^-$]
Ring 1	714 ± 23	1019 ± 37
Ring 2	741 ± 25	1068 ± 51
Ring 3	802 ± 16	1153 ± 48
Ring 4	819 ± 21	1140 ± 26
Ring 5	971 ± 29	1354 ± 57
Ring 6	1081 ± 26	1517 ± 47
Ring 7	1155 ± 38	1681 ± 107

Table 5: The measured ENC in peak and deconvolution mode for different module geometries, in the cold. The uncertainty is the RMS of the resulting ENC distribution per geometry.

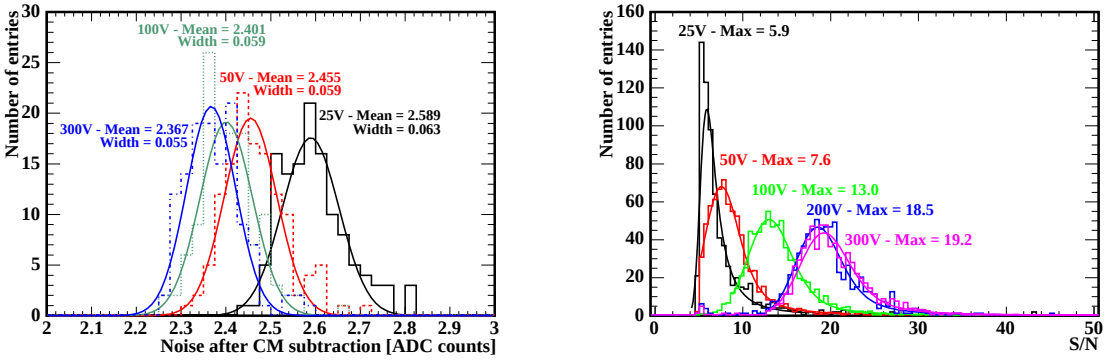

Figure 20: Distributions of the common mode subtracted noise of the first APV (left) and signal-to-noise ratio (right) for the module 4.2 of the back petal for different bias voltages.

5.2.6 Bias Voltage Scans

Several bias voltage scans have been performed to study the effect of the bias voltage on module parameters like noise and cluster width and to determine the minimal bias voltage necessary for full charge collection.
Most of these scans were performed with a muon beam, such that for each scan several modules were hit by the particles. Typically, the bias voltage was raised in steps of 25 V.

Noise

Fig. 20 shows the distributions of the common mode subtracted noise of the first APV of module 4.2 on the back petal and the signal-to-noise ratio of this module for different bias voltages. The effect of the bias voltage is clearly visible.
The mean noise of the first APV of six modules of rings 3 and 4, determined from a Gaussian fit to the noise distributions, is shown in Fig. 21. Due to the higher interstrip capacitance, the noise is increased by about 10 % for the first voltage point (25 V). As expected, for voltages above 75 V and up to 450 V (not shown in the plot), the highest voltage applied, the mean noise is constant.

Plateau voltage

The voltage that must be applied to a module to operate it with optimal S/N is an important parameter. It depends on the thickness and resistivity of the silicon sensors, which, according to the specification document, has to be between 1.5-3.0 kΩcm for thin sensors and between 3.5-7.5 kΩcm for thick sensors [32].
Below the depletion voltage, the signal itself depends linearly on the depletion depth, which in turn depends on the

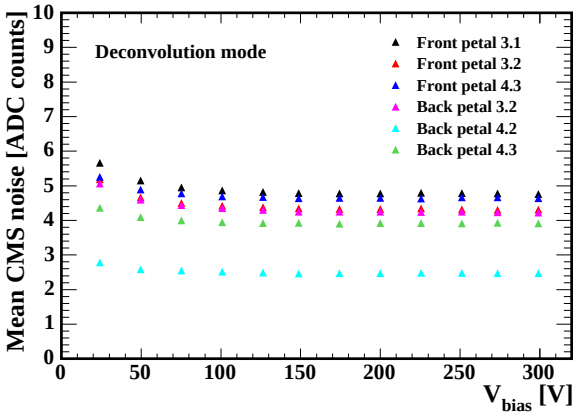

Figure 21: The mean noise of the first APV of six modules of ring 3 and 4 versus the bias voltage.

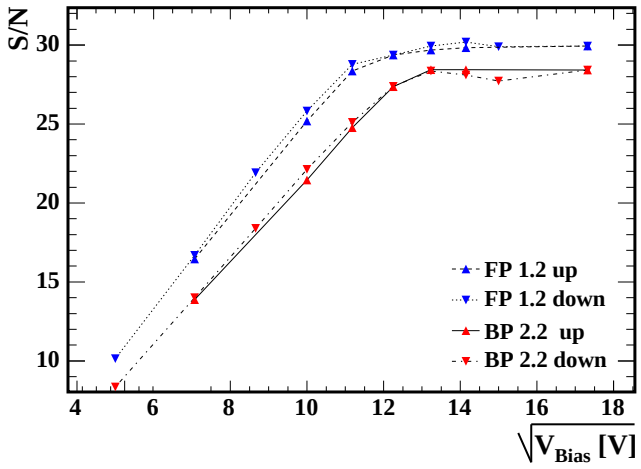

Figure 22: Signal-to-noise ratio versus the square root of the bias voltage for two modules. The bias voltage was ramped up first and then ramped down again.

square root of the bias voltage V_{bias} [33]:

$$Q \propto d = \sqrt{2\epsilon\mu_e\rho V_{\mathrm{bias}}}\,. \tag{1}$$

Here Q is the signal charge, d the sensor thickness, ϵ the dielectric constant for silicon, μ_e the electron mobility and ρ the resistivity. The lowest bias voltage for which saturation of the S/N is observed (called plateau voltage in the following) can be determined only with particles. Above the plateau voltage, the signal is constant.
In Figs. 30-43 (g) the results of HV scans are shown for one module per ring and per petal. To be independent of the optical gain, the S/N instead of the signal is plotted [10] versus $\sqrt{V_{\mathrm{bias}}}$. A straight line plus a constant have been fitted to the curves. The point at 25 V has been excluded from the fit, since for such a low bias voltage the noise is not yet constant. The plateau voltage is the voltage for which the S/N starts to become constant (the kink in the curve). The resulting plateau voltages are listed in Tab. 6.
The plateau voltages are compared to the depletion voltages of the silicon sensors, which are determined during the sensor quality assurance procedure from measurements of the total sensor backplane capacitance versus bias voltage [34]. In this measurement the bias voltage is raised up to 350 V in steps of 5 V. The capacitance between the back plane and the bias line is measured at a frequency of 1 kHz. The depletion voltage is determined from a fit to $1/C^2$ with an uncertainty of approximately 10 V. While for most modules the measured plateau voltage corresponds to the sensor measurement within the uncertainty, there are several modules where the measured plateau voltages are considerably lower than the values from the sensor measurement. In particular this effect is observed for modules of rings 1 and 2, and is not yet understood.

Hysteresis

For the modules of ring 1 and 2 the HV scan was performed with increasing and decreasing bias voltage to study a possible hysteresis effect (S/N depending on the history of the bias voltage applied), since such an effect had been observed previously with modules of the Tracker Inner Barrel [35]. No hint of such an effect was observed, as can be seen from Fig. 22, where the S/N during ramp up and ramp down is compared for two modules. The effect seen on TIB modules was finally attributed to an effect of high relative humidity on the interstrip capacitance and interstrip resistance, and therefore it is consistent that no effect is observed with a relative humidity below 5 %, as provided during the beam test.

[10] For rings 1 and 2 the S/N reached in the bias voltage scan is slightly lower than the S/N shown in Figs. 30-33 (e) due to the fact that these scans were performed relatively early during the beam test, with the timing not yet adjusted in an optimal way.

	Front petal		Back petal	
Module	Depletion voltage [V]	Plateau voltage [V]	Depletion voltage [V]	Plateau voltage [V]
1.1	180*	157.0 ± 4.6	177.2	157.7 ± 4.2
1.2	150*	131.0 ± 4.1	190*	153.0 ± 3.3
1.3	190*	154.8 ± 5.3	-	-
1.4	180*	156.5 ± 4.7	-	-
2.1	158.9	141.5 ± 5.4	200*	177.9 ± 3.5
2.2	180*	137.3 ± 6.7	198.6	152.6 ± 4.1
2.3	182.2	181.2 ± 10.4	-	-
2.4	200*	not measured	-	-
3.1	190*	186.5 ± 5.6	information not available	186.5 ± 3.6
3.2	183.3	191.7 ± 5.5	information not available	176.0 ± 2.5
3.3	200*	187.3 ± 7.2	-	-
4.1	176.3	not measured	180*	not measured
4.2	151.3	190.3 ± 6.5	180*	188.5 ± 5.7
4.3	180*	179.4 ± 6.0	180*	190.6 ± 5.2
4.4	126.9	not measured	-	-
5.1	information not available	209.1 ± 3.0	information not available	192.1 ± 131.0
5.2	information not available	254.0 ± 2.8	information not available	not measured
5.3	information not available	188.3 ± 6.6	> 228.1	213.3 ± 8.1
5.4	information not available	251.3 ± 8.7	information not available	201.1 ± 8.3
5.5	-	-	information not available	185.6 ± 7.6
5.6	-	-	information not available	187.1 ± 6.2
6.1	246.6	243.3 ± 21.6	234.5	240.2 ± 38.1
6.2	207.7	253.5 ± 7.6	258.4	231.2 ± 9.0
6.3	236.0	195.6 ± 16.7	222.3	196.3 ± 8.8
6.4	184.3	230.1 ± 35.0	-	-
7.1	231.5	194.2 ± 37.2	224.0	not measured
7.2	133.0	225.0 ± 0.02	254.8	240.2 ± 20.3
7.3	206.4	233.7 ± 24.5	194.5	195.8 ± 56.4
7.4	135.0	189.7 ± 43.8	220.5	243.4 ± 26.7
7.5	203.5	210.5 ± 45.8	130.0	191.0 ± 65.8

Table 6: The depletion voltages from sensor measurements and plateau voltages as determined in the test beam. The uncertainties for the plateau voltages are statistical errors from the fit. For the thin sensors, only 5 % of the sensors are fully characterized in the quality assurance procedure. Therefore for many thin sensors, marked with a *, only results from measurements performed directly at the company (HPK) are available, which are of much reduced precision.

5.2.7 Study of the Zero Suppression Mode

The VME FED has three readout modes:

- Virgin raw mode: the raw data are passed on to the readout unit.
- Pedestal subtraction mode: pedestals and common mode are subtracted and strips are re-ordered according to their physical position on the sensor. Signals from all strips are passed on to the readout unit.
- Zero suppression mode: pedestals and common mode are subtracted and strips are re-ordered according to their physical order. Cluster finding is performed. Only signals from the strips that belong to a cluster are passed on to the readout unit.

The test beam provided the first chance to study the performance of the zero suppression mode (no runs were taken in pedestal subtraction mode). In Fig. 23 (a) the S/N distributions of front petal module 5.1 measured in the two readout modes are directly compared, showing good agreement.
The relative difference in the S/N for the two readout modes is histogrammed for five ring 5 modules in Fig. 23 (b). A bias voltage scan has been performed in both readout modes, and the S/N values are taken from runs at different

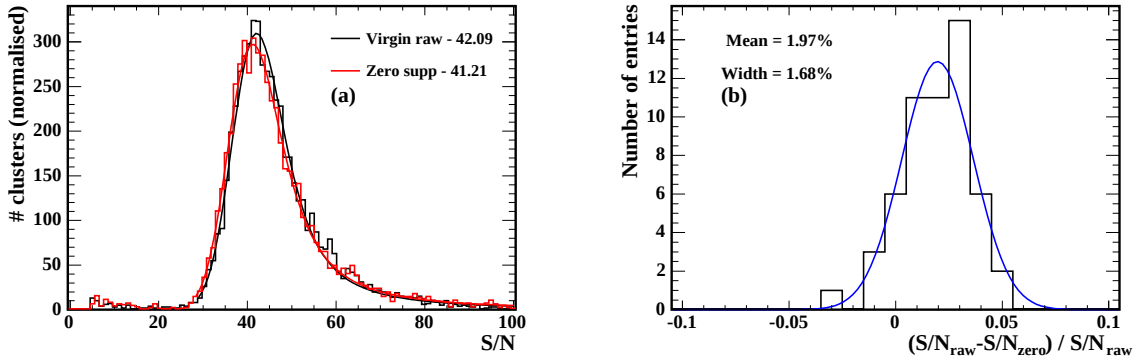

Figure 23: (a) Signal-to-noise ratio in virgin raw and zero suppression mode for module 5.1 on the front petal, and (b) relative difference between the signal-to-noise ratios as determined in virgin raw and zero suppression mode.

bias voltages, i.e. each APV can enter several times into Fig. 23 (b). The S/N in zero suppression mode is smaller by $(2.0 \pm 1.7)\,\%$.

5.2.8 Effect of Leaky Strips

From a certain bias voltage onwards three of the ring 5 modules used in the test beam exhibit a very high noise in one strip, together with a large common mode on the corresponding readout chip. In Fig. 24 the noise distributions in both readout modes are shown for the front petal modules 5.1 and 5.2. The raw noise is clearly distorted in both readout modes, and in peak mode even after common mode subtraction the noise of the affected APV is not completely flat for module 5.1.
The effect strongly depends on the bias voltage, as visible in Fig. 25. While the common mode noise is increased for the affected APV, for the S/N of such APVs the situation is not conclusive: as can be seen from Fig. 26, the S/N of the affected APV is slightly lower for module 5.1, and a small peak of fake clusters with low S/N, caused by very few strips located closely around the noisy strip, is observed. However, for module 5.2 no deterioration of the S/N with respect to the neighbour APVs and no fake clusters are observed.
The effect is observed only on sensors from one out of two suppliers, who will deliver less than 4 % of all sensors of the tracker. About 5 % of the modules built with those sensors are affected. The effect has been attributed to an interplay of a leaky strip drawing a high current and a positive potential difference between the aluminium strip with metal overhang and the implant, causing an electrical field configuration which favours breakdown [36]. It has been shown that the effect is cured by connecting the aluminium strip to ground and pulling the connection of the strip to the APV. Modules known to be affected can thus be fixed. The results presented here show that the signal-to-noise performance of affected modules is not decreased significantly. Modules developing this effect only during operation of the tracker could thus still be operated.

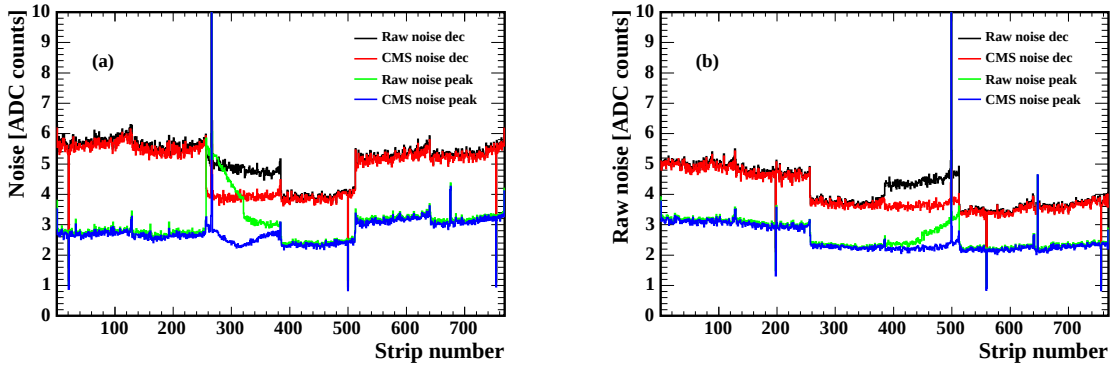

Figure 24: The raw and common mode subtracted noise in peak and deconvolution mode for the modules (a) 5.1 and (b) 5.2 on the front petal.

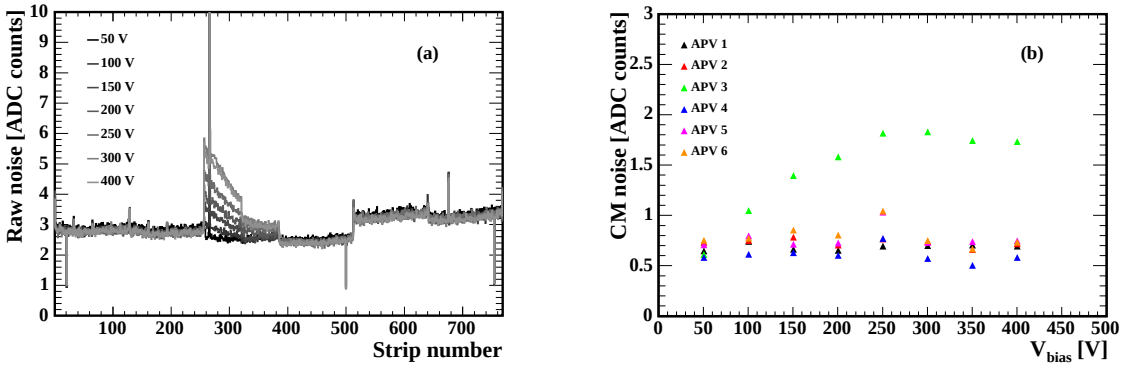

Figure 25: (a) The common mode subtracted noise of front petal module 5.1 in peak mode for several bias voltages, and (b) the common mode noise of all APVs of front petal module 5.1 versus the bias voltage.

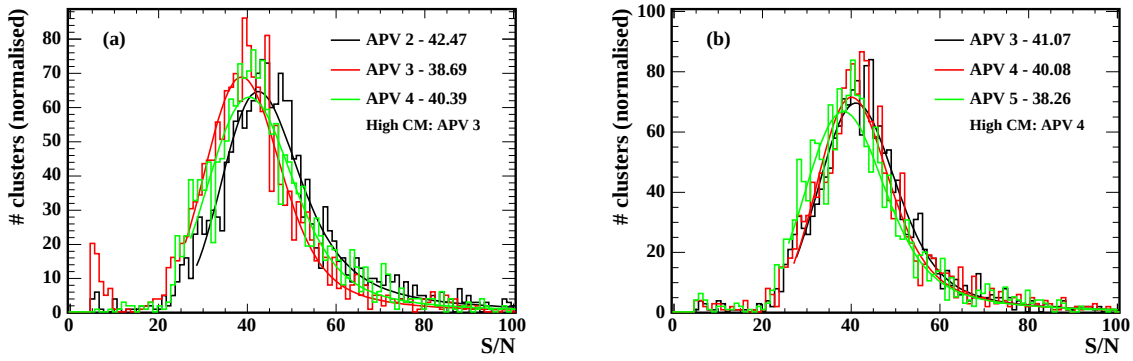

Figure 26: The signal-to-noise distributions of three APVs in peak mode at a bias voltage of 300 V for the modules 5.1 (a) and 5.2 (b) on the front petal.

5.2.9 Hit Efficiency

No beam telescope was available and the petals were mounted without any mechanical precision, so the orientation of the petals with respect to each other as well as the orientation with respect to the beam are not known. Therefore only a rough estimate of the efficiency can be made.
Efficiencies were calculated both for two double-sided ring 5 modules, namely the back petal modules 5.5/5.6 and the front petal modules 5.1/5.2, as well as two double-sided ring 1 modules, namely 1.3/1.4 on the front petal and 1.1/1.2 on the back petal. The chosen double-sided modules of one ring are located behind each other in the beam direction and have a relatively large geometrical overlap.
In the following the individual analysis steps are described:

- From the seed strip numbers of the normal and stereo module and the stereo angle (100 mrad), the hit position in the radial direction (i.e. along the strips) is reconstructed. For each double-sided module a local cartesian coordinate system is used, which has the origin in the geometrical centre of the sensor area of the normal module and the x- and y-axis orthogonal and parallel to the central strips. The three-dimensional pion beam profile on the double-sided module 5.1/5.2 in this local coordinate system is shown in Fig. 27.

- One double-sided module is chosen as the reference module, the other double-sided module is the module "under test".

- To determine the shift of the double-sided modules on the two petals with respect to each other, the distances in the two directions, δx and δy, are calculated for each hit. As can be seen from Fig. 28, in the case of ring 5 the two coordinate systems are shifted by 35.21 mm in x and -13.33 mm in y direction. The hit coordinates of the reference module are corrected for this shift.

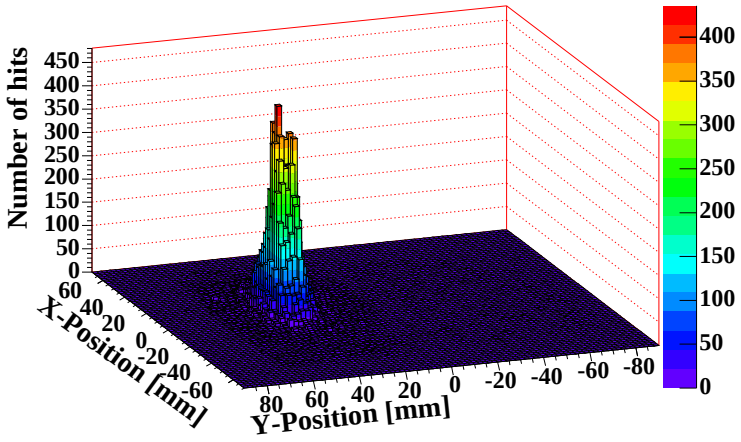

Figure 27: Three-dimensional pion beam profile on modules 5.1 and 5.2 on the front petal.

- On the reference module a rectangular geometrical region is defined such that it is sufficiently far away from the edge of the overlapping region, from physical edges of the sensors of the two individual single-sided modules, and, in case of module 5.5/5.6, from the strips of the dead readout channels of module 5.5. The size of this region is 15 mm x 20 mm for ring 5 and 45 mm x 55 mm for ring 1. For the module 5.5/5.6, the reconstructed hit positions within this region, showing its location in the local coordinate system, can be seen in Fig. 29.
- Only events with exactly one hit in the selected area of the reference module are considered, and to avoid ambiguities in computing the hit position, events are disregarded if they do not have exactly one hit on both the normal and stereo reference module.
- For events with a hit in the selected region of the reference module, the hit positions on the module under test are reconstructed. As visible from Fig. 29 for the case of ring 5, these hits are located within a parallelogram. This reflects the fact that the two double-sided R5 modules are not only shifted but also rotated with respect to each other. From the shape of the parallelogram, a rotation angle of $5.4°$ is calculated. The hit positions on the reference module are corrected for this rotation. For ring 1, the two double-sided modules are rotated by $2.3°$ with respect to each other.
- The widths of the δx and δy distributions after rotation represent the spatial resolutions in the two directions. For the case of ring 5, the resolutions are 99.7 μm in x direction, i.e. orthogonal to the strips, and 991.6 μm in y direction, i.e. along the strips. For ring 1 the corresponding numbers are 115 μm and 630 μm, respectively.
- The beam is assumed to be orthogonal to the sensor areas of the hit detectors, thus the computed hit position of the reference module is also the predicted hit position for the double-sided module under test.

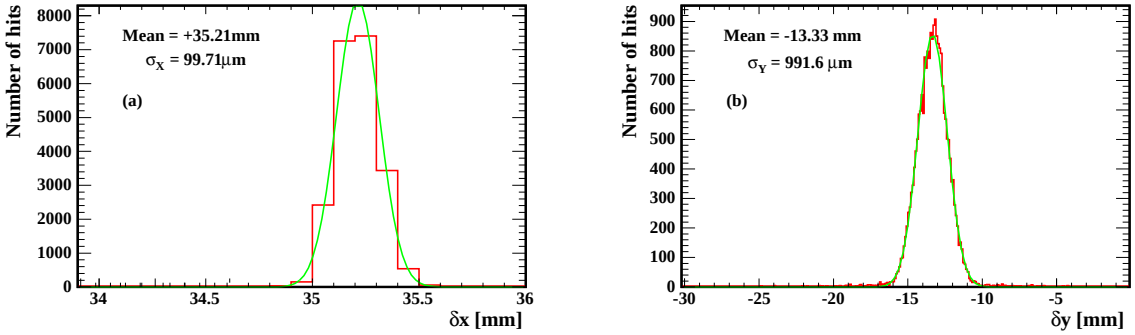

Figure 28: Distance between the hit coordinates of the double-sided module 5.1/5.2 on the front petal and 5.5/5.6 on the back petal (after rotation of the reference hits by $5.4°$): (a) δx and (b) δy.

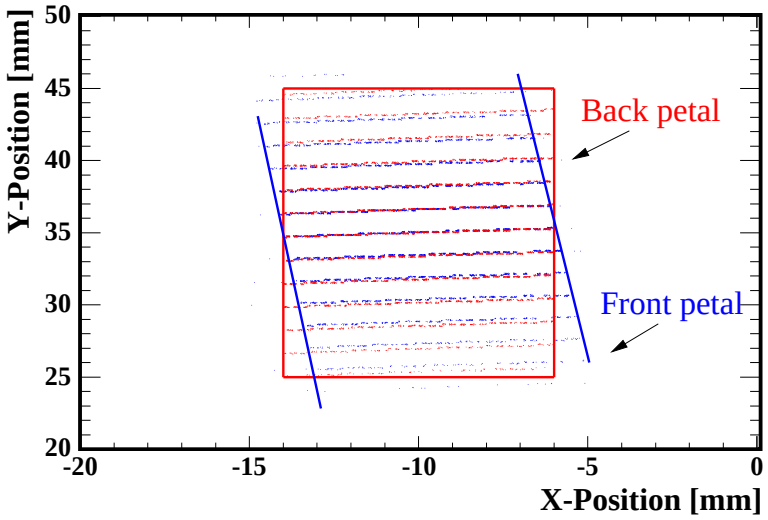

Figure 29: Reconstructed coordinates on the back petal module 5.5/5.6 (used as the reference module) and the front petal module 5.1/5.2, before rotation. The lines are drawn by hand to guide the eye.

- On all modules bad strips are present. For the reference module, the two nearest neighbour strips on each side of a bad strip, i.e. four strips in total, are excluded for the efficiency calculation. Furthermore it is checked if the predicted hit location on the module under test is within a two-strip wide region around a bad strip. If this is the case, the event is not used in the calculation.
- For each of the two modules of the double-sided module under test, the number of events with a hit not further than two strips away from the predicted strip are counted. This gives samples of candidate events $N^i_{\text{candidate}}$ and $N^j_{\text{candidate}}$, in which the particle was seen in module i or j and thus has certainly traversed the remaining module j or i, respectively.
- For each candidate, corresponding hits on the module under test are searched for, and are considered as matching hits if they are located not more than three times the resolution for ring 5 and four times the resolution for ring 1 away from the predicted area (N_{sel}). Rings 5 and 1 are treated differently because larger incident angles are expected on ring 1. This is due to the fact that the high-statistic runs used for this study were taken with a muon beam on ring 1, while a pion beam was present on ring 5. Furthermore, a larger geometrical area is used on ring 1 to increase the statistics.
- Finally the efficiency ϵ_i of the module i under test is given by the number of events where a matching hit is found on the double-sided module, divided by the number of events where the the partner module has seen a hit: $\epsilon_i = N_{\text{sel}}/N^j_{\text{candidate}}$.

The resulting efficiencies of all studied modules are summarized in the second column of Tab. 7. Efficiencies above 99 % are found. The large common mode present on single APVs on modules 5.1 and 5.2 (Sect. 5.2.8) does not deteriorate the hit efficiency. With a statistics of about 10000 events on ring 5 and 3500 events on ring 1, the statistical uncertainty amounts to about 1.4 % on ring 5 and about 2.4 % on ring 1. The observed differences between modules have therefore no significance.
The effect of bad strips on the hit efficiency has been studied by unmasking different numbers of bad strips. The loss in efficiency corresponds roughly to the fraction of bad strips.
For the ring 5, efficiencies have also been calculated for data obtained in zero suppression mode (third column of Tab. 7). About 4000 events have been used for this study. No significant effect of the FED readout mode on the efficiency is observed.

6 Summary

In May/June 2004, a full TEC control loop, consisting of a front and a back petal, was operated and tested in muon and pion particle beams at CERN. With its 51 silicon modules this was the largest substructure of the CMS silicon

Module	Efficiency Virgin raw mode	Efficiency Zero suppression mode
FP 5.1	99.2 %	99.4 %
FP 5.2	99.2 %	99.4 %
BP 5.5	99.1 %	99.1 %
BP 5.6	98.6 %	99.1 %
FP 1.3	99.5 %	-
FP 1.4	99.4 %	-
BP 1.1	99.7 %	-
BP 1.2	99.6 %	-

Table 7: Efficiencies for the modules studied, with data obtained in virgin raw and zero suppression mode.

strip tracker tested so far. Stable system operation was achieved both at room temperature and at temperatures compatible with CMS operating conditions.
Most probable values for the signal-to-noise ratio of 28-33 (35-42) in peak mode and 19-22 (20-24) in deconvolution mode have been observed for thin (thick) sensors. Noise distributions of all modules were studied, and the equivalent noise charge has been determined per geometry. The ENC was found to be between 714 and 1155 electrons in peak mode and between 1020 and 1681 electrons in deconvolution mode. A mean common mode noise of (173 ± 38) electrons in peak and (299 ± 76) electrons in deconvolution mode was measured. A decrease in the noise of about 10 % was observed between room temperature and CMS operating conditions. All numbers quoted above have been obtained in the cold environment.
With the excellent performance described above the operation of a TEC control loop in the test beam 2004 was a major step towards working tracker end caps in 2007.

Acknowledgements

The authors would like to express their gratitude to all the people from the test beam support team, especially L. Mirabito, who developed and set up the data acquisition environment, J. Fulcher, M. Noy and M. Pearson, who helped us to operate the FED, F. Drouhin, L. Gross, and D. Vintache from the FEC support, St. Dris and J. Troska for their help with questions related to the optical components, and E. Carrone and A. Tsirou for providing the interlock. A special "thank you" goes to P. Siegrist for the organisation and his overall support.

References

[1] L. Borello, E. Focardi, A. Macchiolo and A. Messineo, *Sensor design for the CMS Silicon Strip Tracker*, CMS Note 2003/020 (2003).

[2] CMS Collaboration, *The Tracker Project, Technical Design Report*, CERN/LHCC 98-6, CMS TDR 5 (15. April 1998).

[3] CMS Collaboration, *Addendum to the CMS Tracker TDR*, CERN/LHCC 2000-016, CMS TDR 5 Addendum 1 (21. April 2000).

[4] G. Cervelli *et al.*, Nucl. Instrum. and Methods **A466** (2001) 359.

[5] U. Goerlach, *Industrial production of Front-End Hybrids for the CMS Silicon Tracker*, Proc. of the 9th Workshop on Electronics for LHC experiments, Amsterdam, Netherlands (2003).

[6] S. Gadomski, H. Hall, T. Høgh, P. Jalocha, E. Nygård and P. Weilhammer, Nucl. Instrum. and Methods **A320** (1992) 217.

[7] G. Cervelli, A. Marchioro, P. Moreira and F. Vasey, *A radiation tolerant laser driver array for optical transmission in the LHC experiments*, Proc. of the 6th Workshop on Electronics for LHC Experiments, Krakow, Poland (2000).

[8] J. Troska *et al.*, IEEE Trans. Nucl. Sci. **50** (2003) 1067.

[9] J.A. Coughlan, *The Front-End Driver card for the CMS Silicon Tracker Readout*, Proc. of the 8th Workshop on Electronics for LHC experiments, Colmar, France (2002).

[10] B.G. Taylor for the RD12 Coll., IEEE Trans. Nucl. Sci. **45** (1998) 821.

[11] K. Gill, G. Dewhirst, R. Grabit, J. Troska and F. Vasey, *80 Mbit/s Digital Optical Links for Control, Timing and Trigger of the CMS Tracker*, Proc. of the 8th Workshop on Electronics for LHC experiments, Colmar, France (2002).

[12] C. Ljuslin, M. Marchioro and C. Paillard, *The CCU25: a network oriented Communication and Control Unit integrated circuit in a 0.25 μm CMOS technology*, Proc. of the 8th Workshop on Electronics for LHC experiments, Colmar, France (2002).

[13] K. Kloukinas, A. Marchioro, P., Moreira and P. Placidi, *A 40 MHz clock and trigger recovery circuit for the CMS tracker fabricated in a 0.25 μm CMOS technology and using a self calibration technique*, LEB electronics workshop 1999, Snowmass (1999).

[14] http://www.semiconductors.philips.com/buses/i2c/

[15] G. Magazzu, A. Marchioro, P. Moreira, IEEE Trans. Nucl.Sci. **51** (2004) 1333.

[16] http://ab-dep-op-sps.web.cern.ch/ab-dep-op-sps/

[17] The CMS TriDAS Coll., *Clustered Data Acquisition for the CMS experiment*, Proc. of the International Conference on Computing in High Energy and Nuclear Physics, Beijing (2001).

[18] CMS Collaboration, *The Trigger and Data Acquisition Project, Volume II, Data Acquisition & High-Level Trigger, Technical Design Report*, CERN/LHCC 2002-26, CMS TDR 6.2 (15. December 2002).

[19] A.S. Johnson, SLAC-PUB-7963 (1998).

[20] R. Brun and F. Rademakers, Nucl. Instrum. and Methods **A389** (1997) 81.

[21] http://st-support-cooling-electronics.web.cern.ch/st-support-cooling-electronics/CWGWeb/TABLE4-1.HTM

[22] http://accms04.physik.rwth-aachen.de/~cms/Tracker/Electronics/Drawings/cablings/data/Cables_x-sec_Al-Cu.pdf

[23] K. Gill, L. Mirabito and B. Trocme, *Synchronization of the CMS Tracker*, Proc. of the 9th Workshop on Electronics for LHC experiments, Amsterdam, Netherlands (2003).

[24] R. Brauer, *Systemtests an modernen Detektoren in der Teilchenphysik*, Diploma thesis, I. Physikalisches Institut B, RWTH Aachen (2004).
Updates of the analysis are described on http://brauer.home.cern.ch/brauer/Ana/index.html

[25] V. Innocente *et al.*, *The Design, Implementation and Deployment of a Functional Prototype OO Reconstruction Software for CMS. The ORCA Project.*, Proc. of CHEP 2000, Padova, Italy (2000).

[26] M. Raymond, private communication.

[27] S. Dris *et al.*, *Predicting the In-System Performance of the CMS Tracker Analogue Readout Optical Links*, Proc. of the 10th Workshop on Electronics for LHC Experiments, Boston, USA (2004).

[28] http://abbaneo.home.cern.ch/abbaneo/cms/layout/forw_final/w6_3.result

[29] M.M. Angarano *et al.*, *Study of radiation damage and substrate resistivity effects from beam test of silicon microstrip detectors using LHC readout electronics*, CMS Note 2000/053 (2000);
S. Albergo *et al.*, *High Voltage Operation of Heavily Irradiated Silicon Microstrip Detectors*, CMS CR 1999/019 (1999).

[30] M. Raymond *et al.*, *The CMS Tracker APV25 0.25 μm CMOS Readout Chip*, Proc. of the 6th Workshop on Electronics for LHC Experiments, Krakow, Poland (2000).

[31] E.A. Noah Messomo, *Radiation and Temperature Effects on the APV25 Readout Chip for the CMS Tracker*, Doctoral Thesis, Imperial College London (2002).

[32] Supply of Silicon Micro-Strip Sensors for The CMS Silicon Strip Tracker (SST), Invitation to Tender: IT-2777/EP/CMS, Technical Specification, November 2000.

[33] G. Lutz, *Semiconductor Radiation Detectors*, ISBN 3-540-64859-3 (1999).

[34] J.L. Agram *et al.*, *The Silicon Sensors for the Compact Muon Solenoid Tracker - Design and Qualification Procedure*, CMS Note 2003/015 (2003).

[35] A. Macchiolo, private communication.

[36] G. Tonelli, private communication.

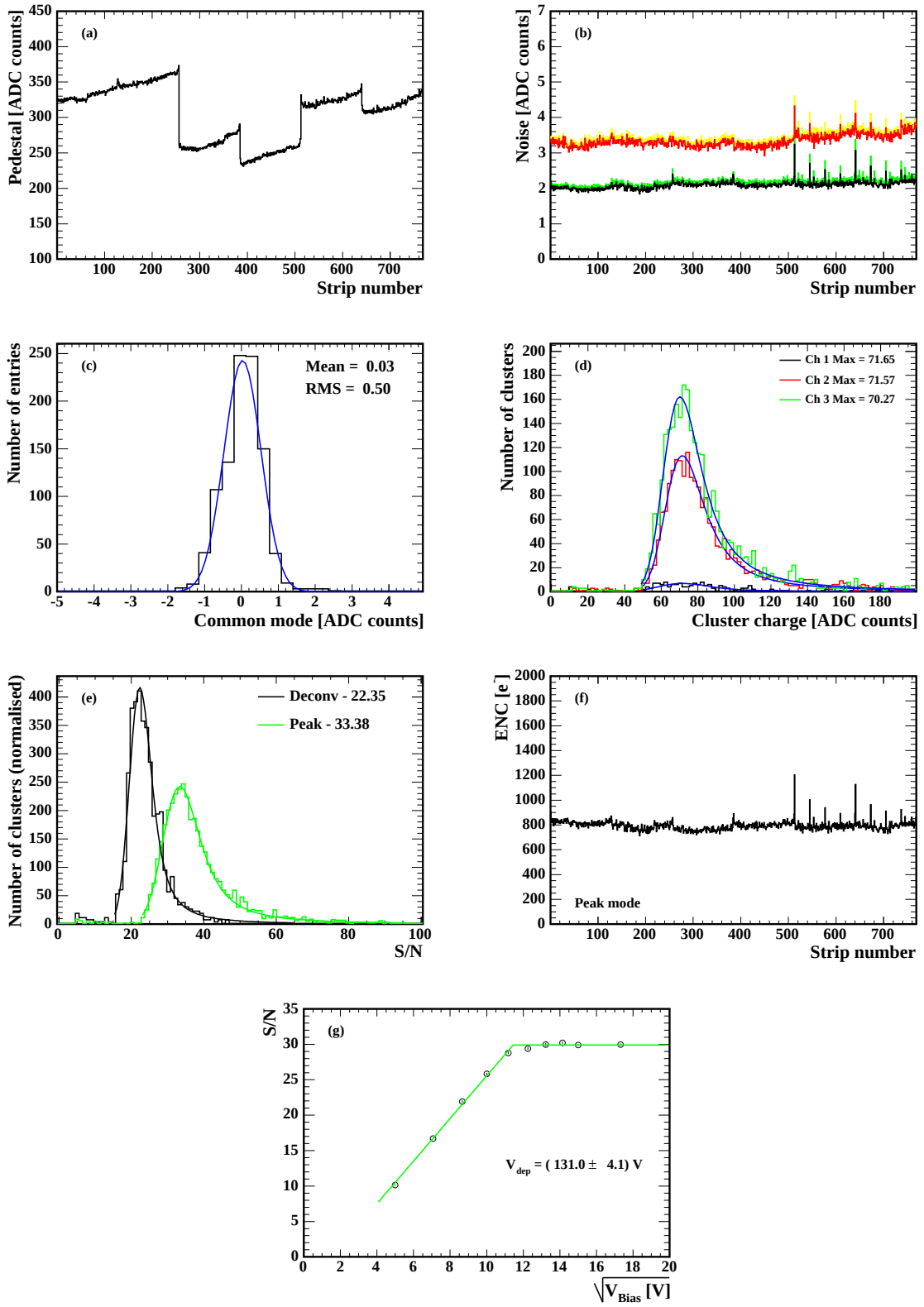

Figure 30: Characteristic distributions for a ring 1 module (module 1.2) on the front petal: (a) pedestal distribution, (b) raw and common mode subtracted noise for peak (green and black curves) and deconvolution mode (yellow and red curves), (c) common mode of the first APV in peak mode, (d) the cluster charge distribution in peak mode for each optical channel, (e) normalized distributions of the signal-to-noise ratio for peak (green/light grey) and deconvolution mode (black), (f) ENC in peak mode, (g) bias voltage scan.
All measurements were made in the cold environment.
The spike structure in the noise distribution of the third optical channel is present not in all runs, and is probably due to non-optimal readout synchronisation.

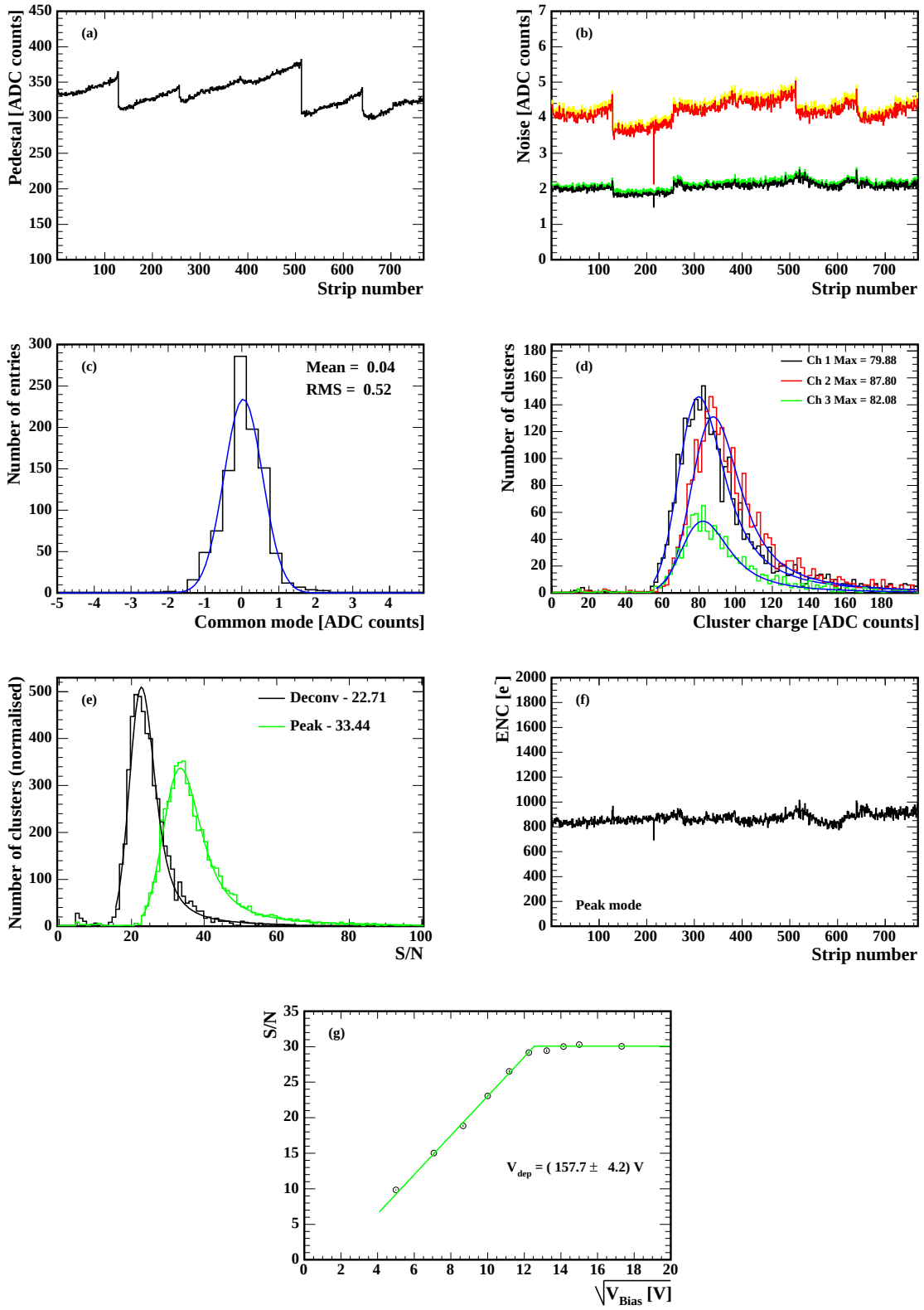

Figure 31: Characteristic distributions for a ring 1 module (module 1.1) on the back petal: (a) pedestal distribution, (b) raw and common mode subtracted noise for peak (green and black curves) and deconvolution mode (yellow and red curves), (c) common mode of the first APV in peak mode, (d) the cluster charge distribution in peak mode for each optical channel, (e) normalized distributions of the signal-to-noise ratio for peak (green/light grey) and deconvolution mode (black), (f) ENC in peak mode, (g) bias voltage scan.
All measurements were made in the cold environment.

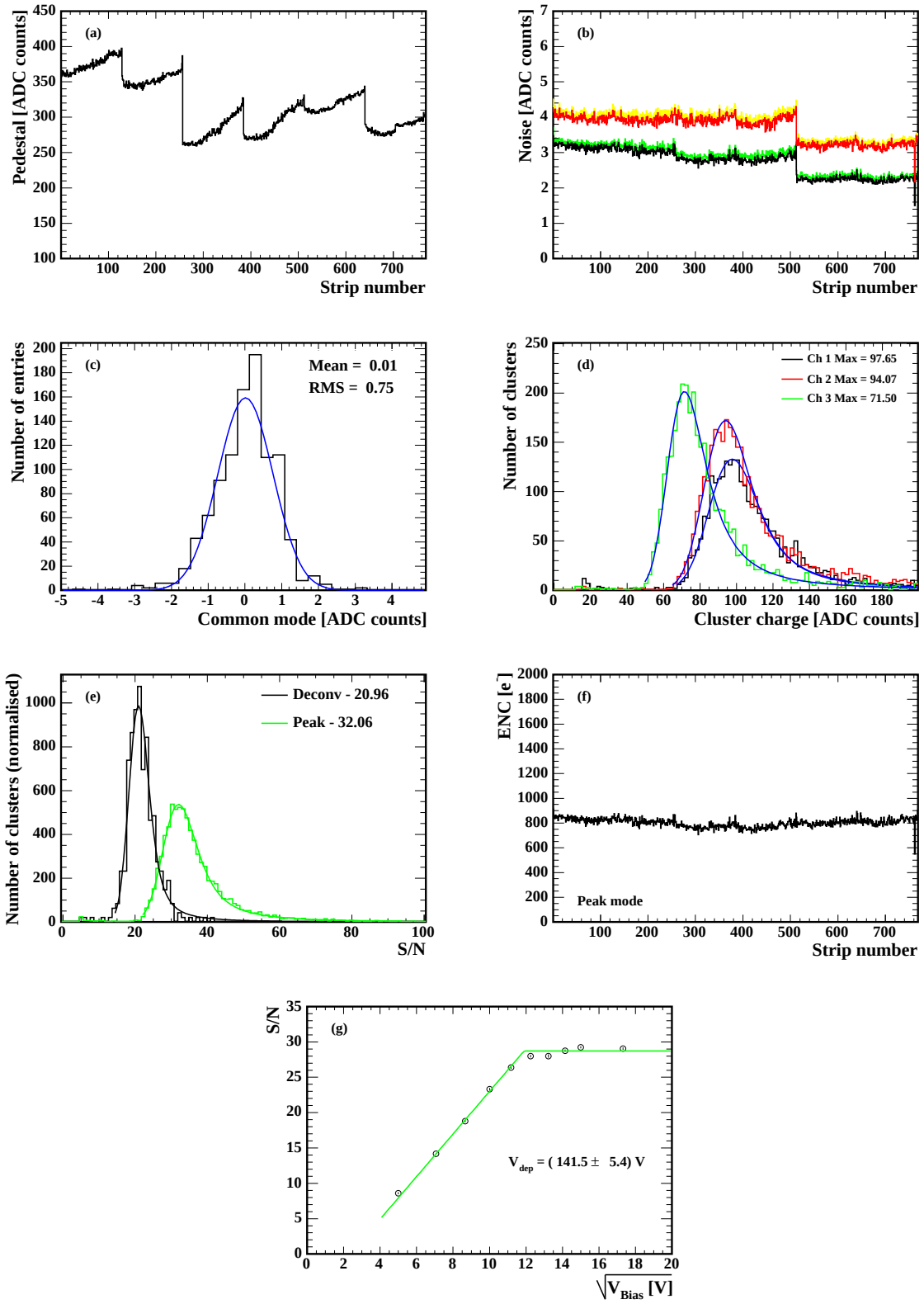

Figure 32: Characteristic distributions for a ring 2 module (module 2.1) on the front petal: (a) pedestal distribution, (b) raw and common mode subtracted noise for peak (green and black curves) and deconvolution mode (yellow and red curves), (c) common mode of the first APV in peak mode, (d) the cluster charge distribution in peak mode for each optical channel, (e) normalized distributions of the signal-to-noise ratio for peak (green/light grey) and deconvolution mode (black), (f) ENC in peak mode, (g) bias voltage scan.
All measurements were made in the cold environment.

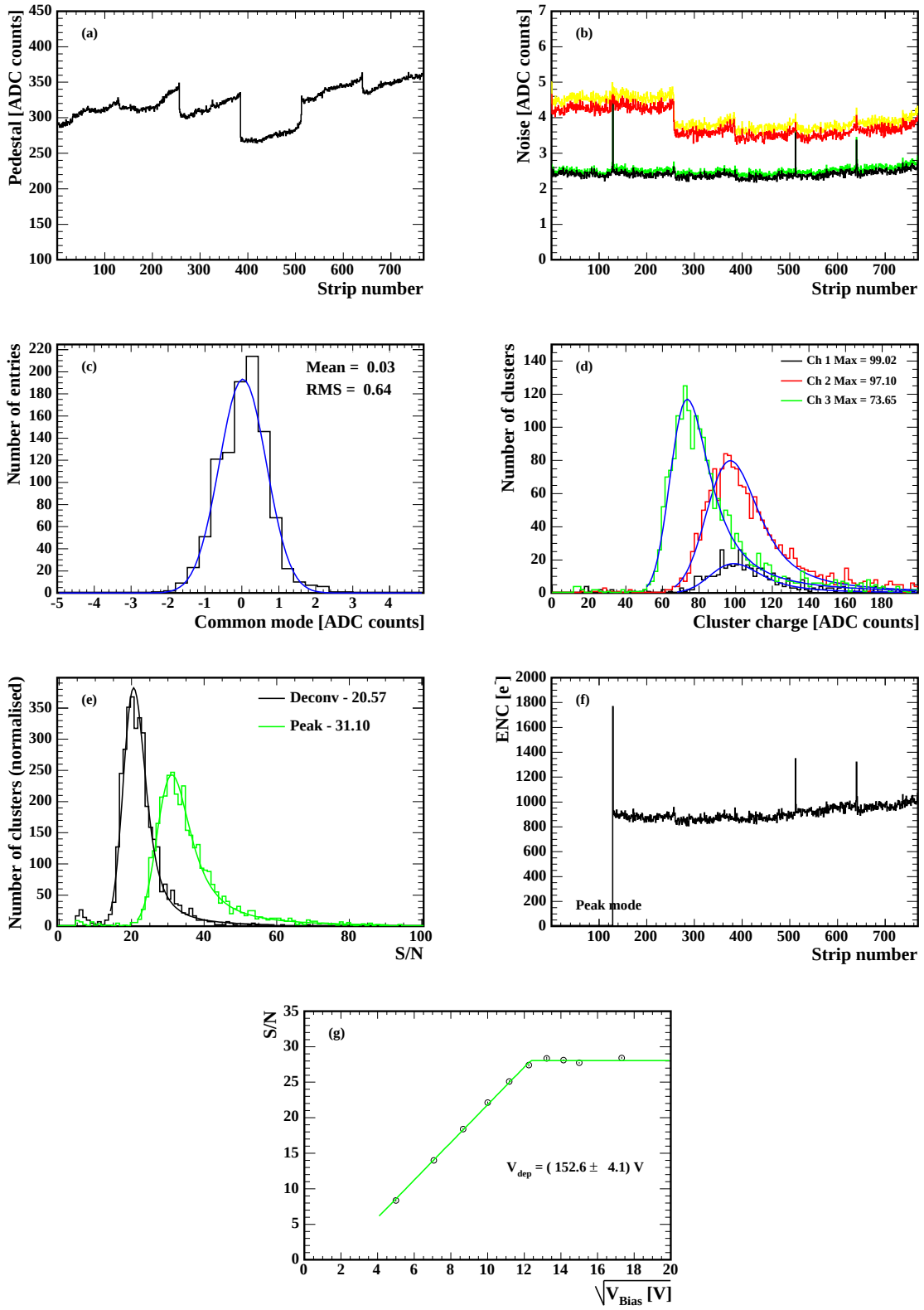

Figure 33: Characteristic distributions for a ring 2 module (module 2.2) on the back petal: (a) pedestal distribution, (b) raw and common mode subtracted noise for peak (green and black curves) and deconvolution mode (yellow and red curves), (c) common mode of the first APV in peak mode, (d) the cluster charge distribution in peak mode for each optical channel, (e) normalized distributions of the signal-to-noise ratio for peak (green/light grey) and deconvolution mode (black), (f) ENC in peak mode, (g) bias voltage scan.
All measurements were made in the cold environment.
Due to low data statistics the ENC was not calculated for APV1.

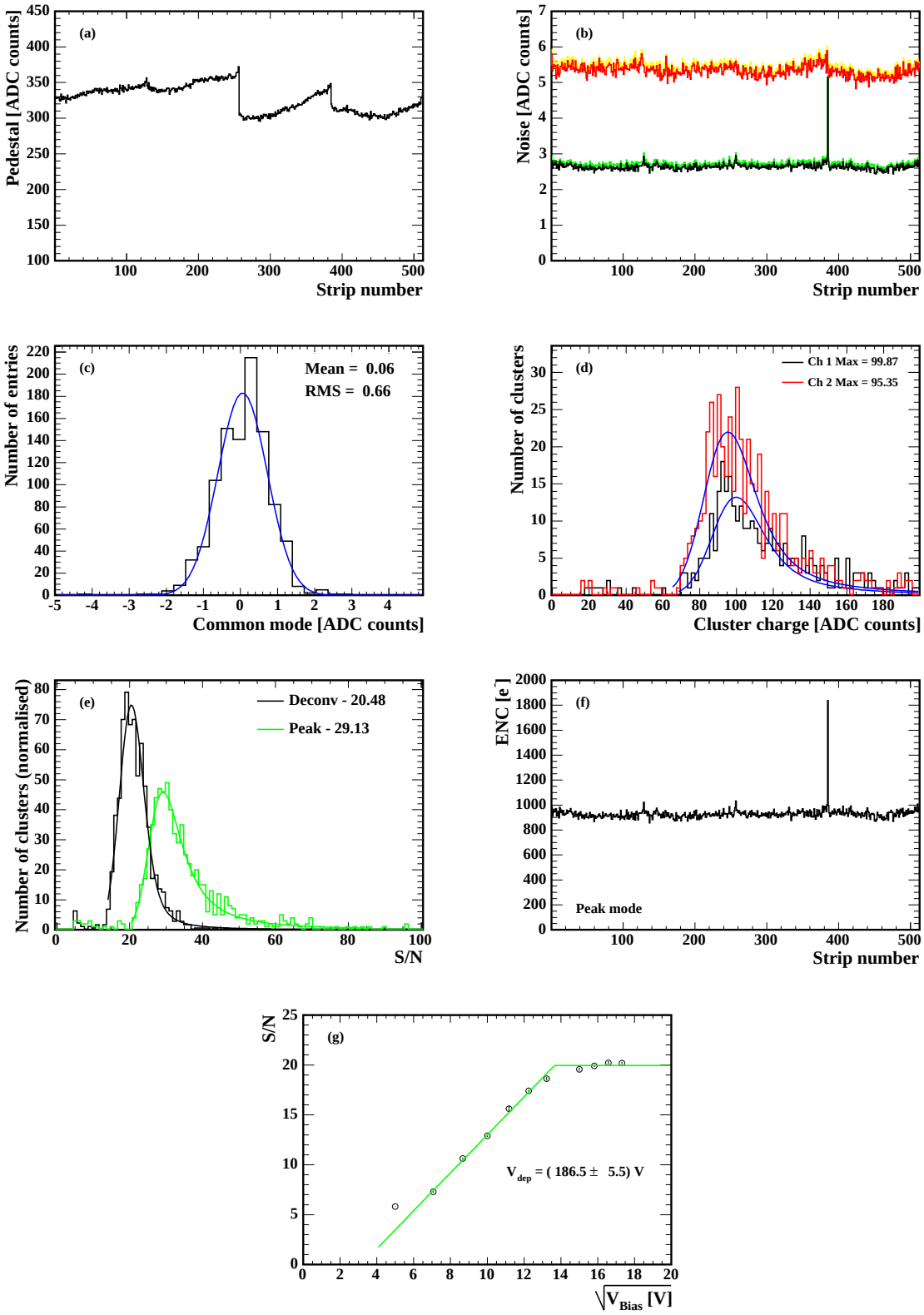

Figure 34: Characteristic distributions for a ring 3 module (module 3.1) on the front petal: (a) pedestal distribution, (b) raw and common mode subtracted noise for peak (green and black curves) and deconvolution mode (yellow and red curves), (c) common mode of the first APV in peak mode, (d) the cluster charge distribution in peak mode for each optical channel, (e) normalized distributions of the signal-to-noise ratio for peak (green/light grey) and deconvolution mode (black), (f) ENC in peak mode, (g) bias voltage scan.
All measurements were made in the cold environment.

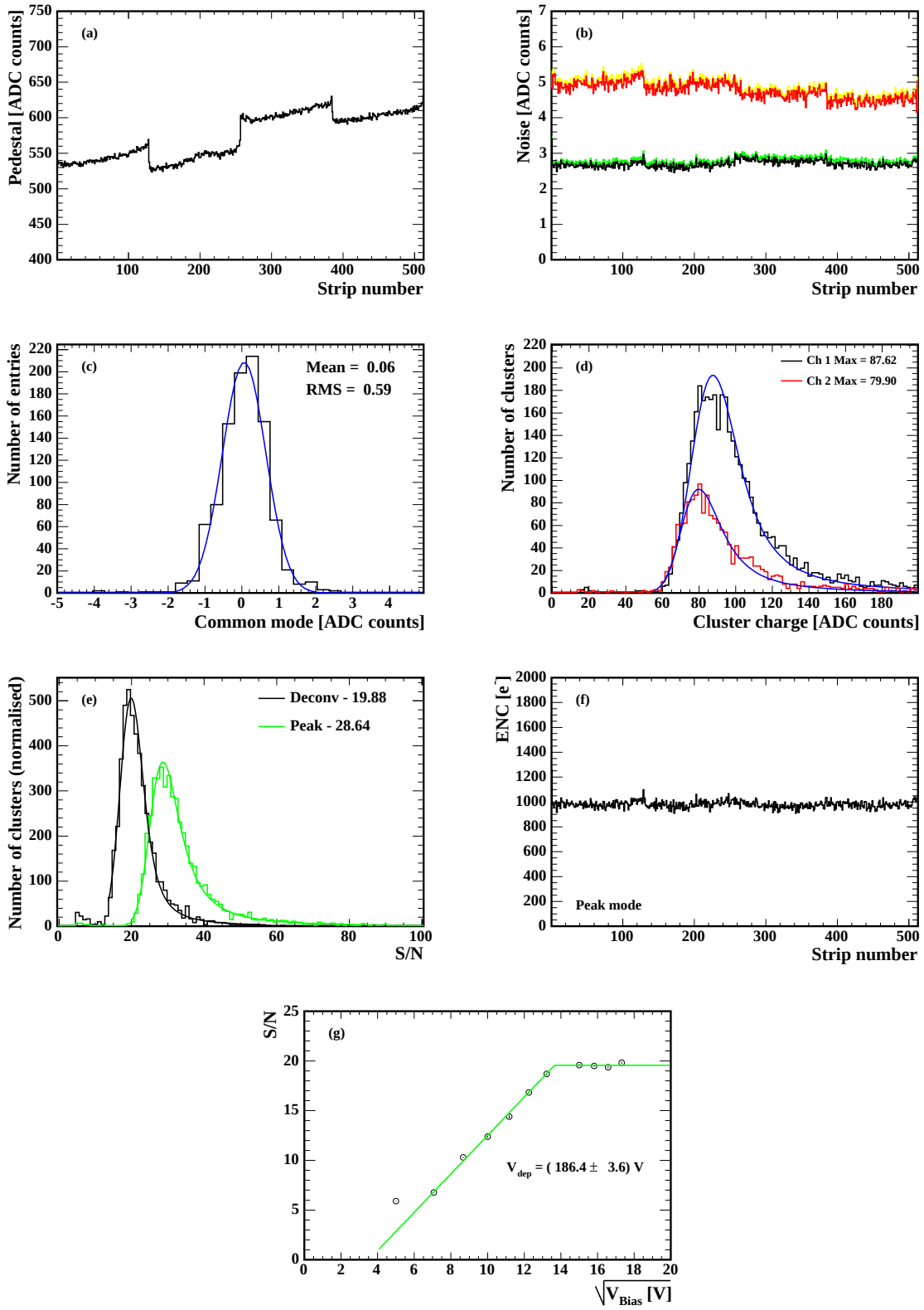

Figure 35: Characteristic distributions for a ring 3 module (module 3.1) on the back petal: (a) pedestal distribution, (b) raw and common mode subtracted noise for peak (green and black curves) and deconvolution mode (yellow and red curves), (c) common mode of the first APV in peak mode, (d) the cluster charge distribution in peak mode for each optical channel, (e) normalized distributions of the signal-to-noise ratio for peak (green/light grey) and deconvolution mode (black), (f) ENC in peak mode, (g) bias voltage scan.
All measurements were made in the cold environment.

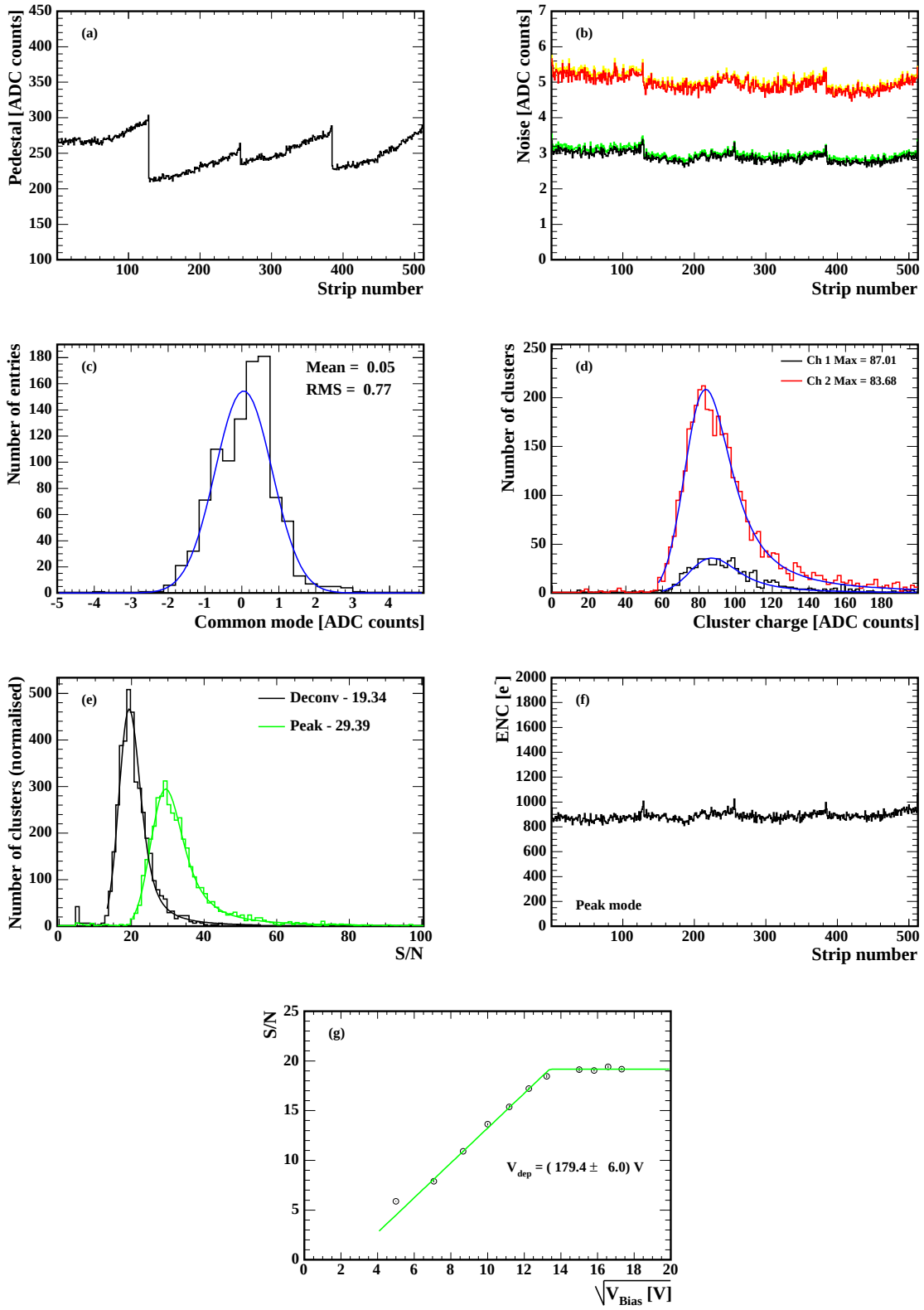

Figure 36: Characteristic distributions for a ring 4 module (module 4.3) on the front petal: (a) pedestal distribution, (b) raw and common mode subtracted noise for peak (green and black curves) and deconvolution mode (yellow and red curves), (c) common mode of the first APV in peak mode, (d) the cluster charge distribution in peak mode for each optical channel, (e) normalized distributions of the signal-to-noise ratio for peak (green/light grey) and deconvolution mode (black), (f) ENC in peak mode, (g) bias voltage scan.
All measurements were made in the cold environment.

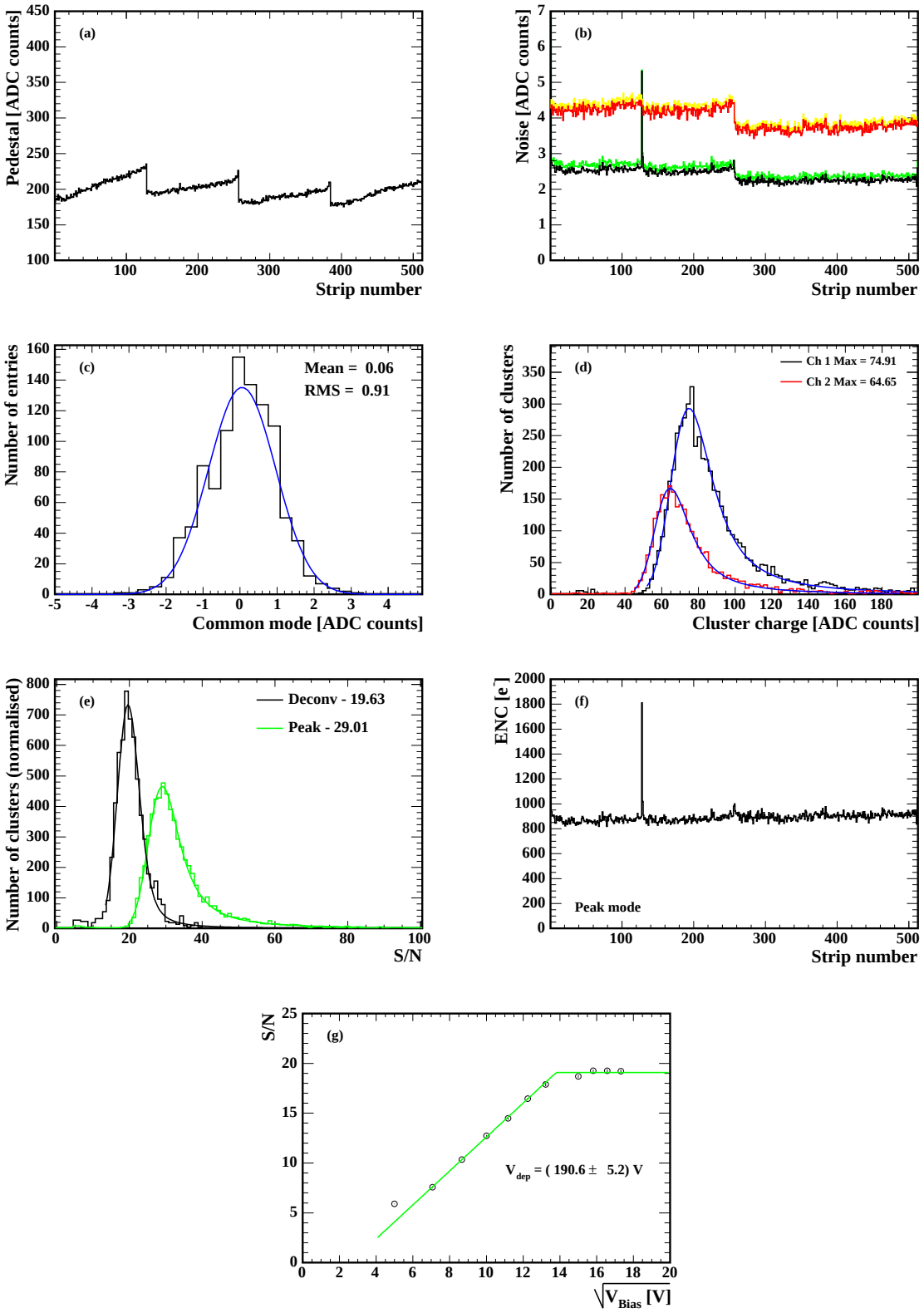

Figure 37: Characteristic distributions for a ring 4 module (module 4.3) on the back petal: (a) pedestal distribution, (b) raw and common mode subtracted noise for peak (green and black curves) and deconvolution mode (yellow and red curves), (c) common mode of the first APV in peak mode, (d) the cluster charge distribution in peak mode for each optical channel, (e) normalized distributions of the signal-to-noise ratio for peak (green/light grey) and deconvolution mode (black), (f) ENC in peak mode, (g) bias voltage scan.
All measurements were made in the cold environment.

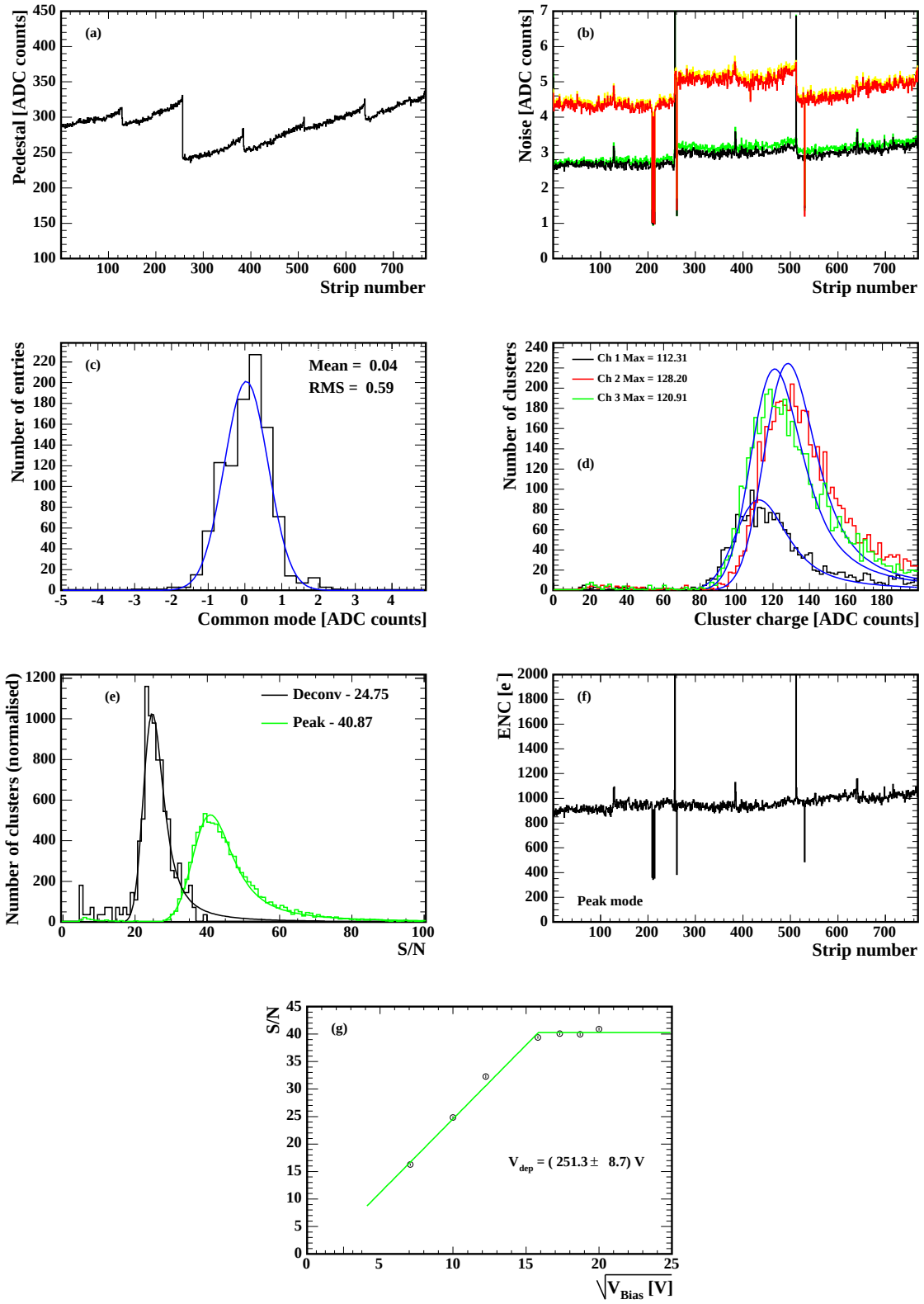

Figure 38: Characteristic distributions for a ring 5 module (module 5.4) on the front petal: (a) pedestal distribution, (b) raw and common mode subtracted noise for peak (green and black curves) and deconvolution mode (yellow and red curves), (c) common mode of the first APV in peak mode, (d) the cluster charge distribution in peak mode for each optical channel, (e) normalized distributions of the signal-to-noise ratio for peak (green/light grey) and deconvolution mode (black), (f) ENC in peak mode, (g) bias voltage scan.
All measurements were made in the cold environment.

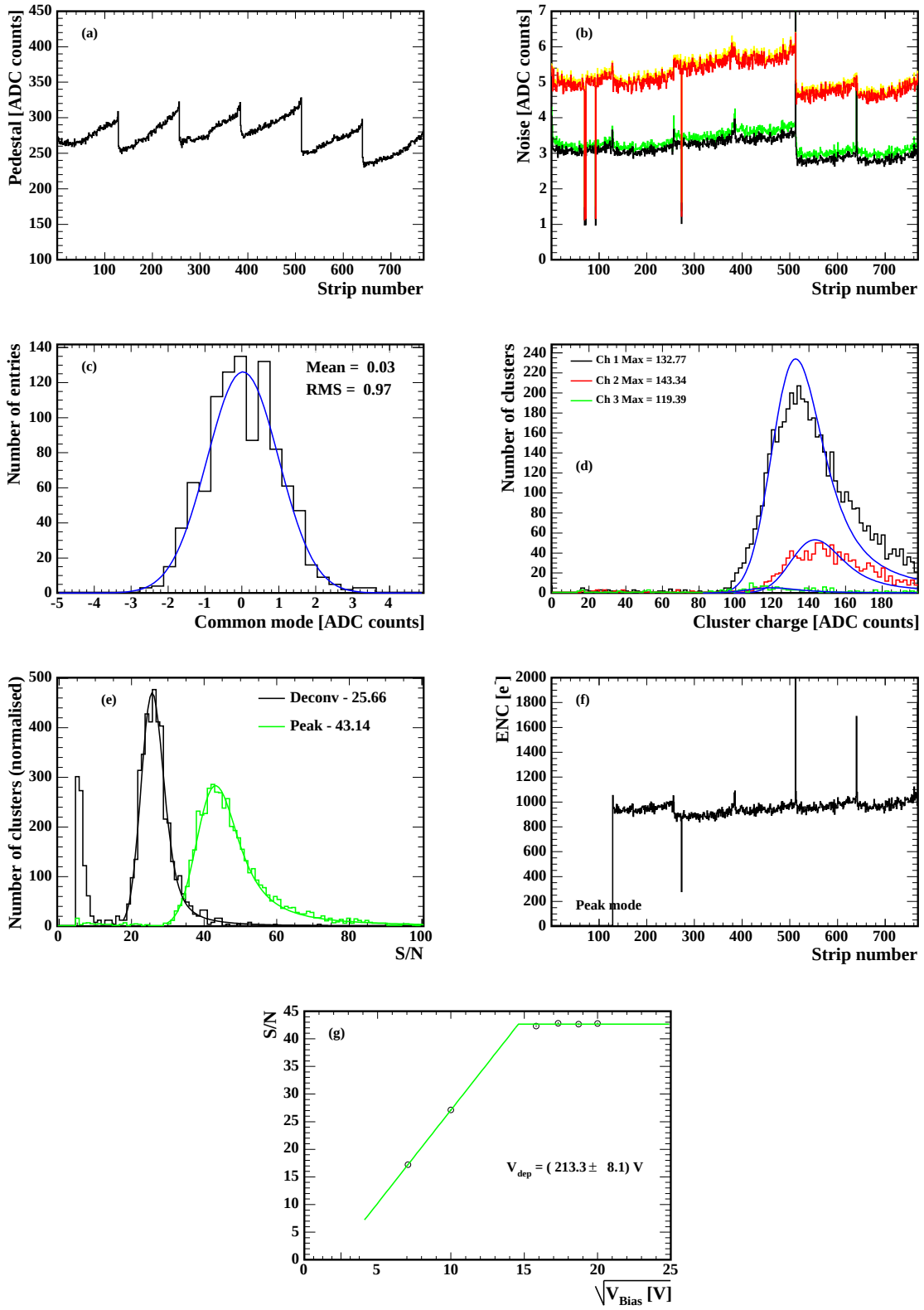

Figure 39: Characteristic distributions for a ring 5 module (module 5.3) on the back petal: (a) pedestal distribution, (b) raw and common mode subtracted noise for peak (green and black curves) and deconvolution mode (yellow and red curves), (c) common mode of the first APV in peak mode, (d) the cluster charge distribution in peak mode for each optical channel, (e) normalized distributions of the signal-to-noise ratio for peak (green/light grey) and deconvolution mode (black), (f) ENC in peak mode, (g) bias voltage scan.
All measurements were made in the cold environment. Due to low data statistics the ENC was not calculated for APV1. The peak of clusters with low S/N in deconvolution mode in (e) is due to particles from the previous bunch crossing of the LHC-like pion beam that are sampled at their tail.

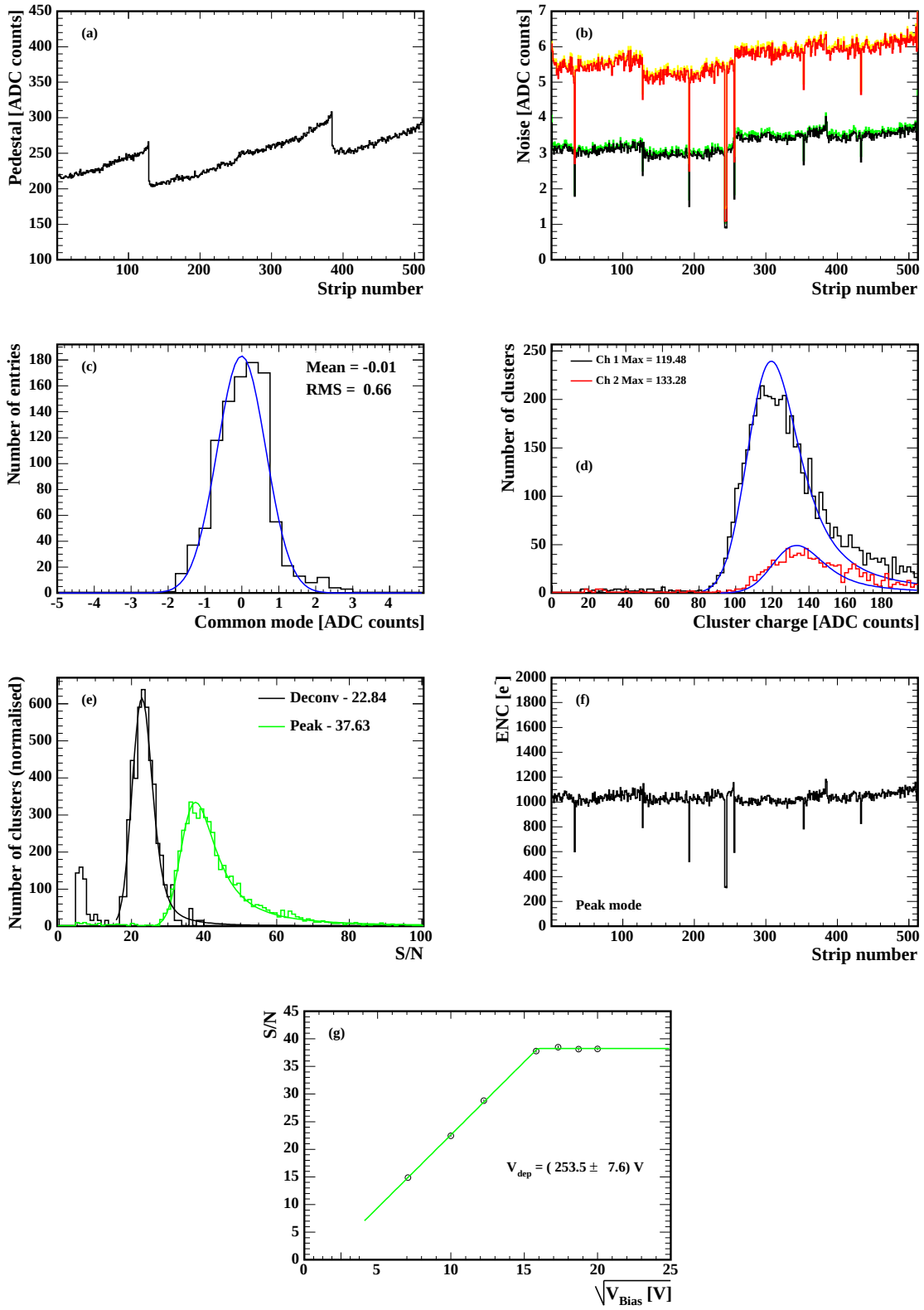

Figure 40: Characteristic distributions for a ring 6 module (module 6.2) on the front petal: (a) pedestal distribution, (b) raw and common mode subtracted noise for peak (green and black curves) and deconvolution mode (yellow and red curves), (c) common mode of the first APV in peak mode, (d) the cluster charge distribution in peak mode for each optical channel, (e) normalized distributions of the signal-to-noise ratio for peak (green/light grey) and deconvolution mode (black), (f) ENC in peak mode, (g) bias voltage scan.
All measurements were made in the cold environment.
The peak of clusters with low S/N in deconvolution mode in (e) is due to particles from the previous bunch crossing of the LHC-like pion beam that are sampled at their tail.

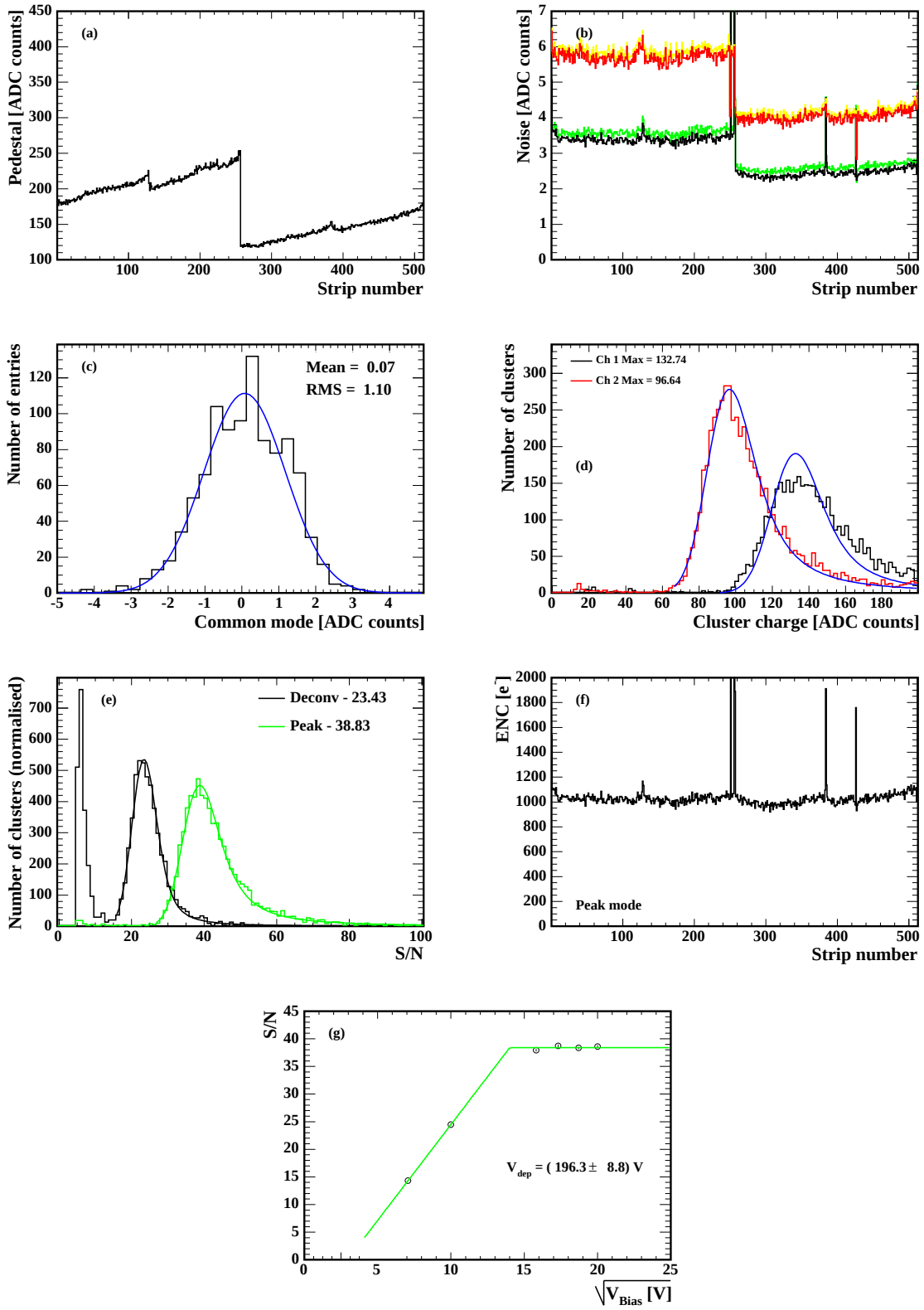

Figure 41: Characteristic distributions for a ring 6 module (module 6.3) on the back petal: (a) pedestal distribution, (b) raw and common mode subtracted noise for peak (green and black curves) and deconvolution mode (yellow and red curves), (c) common mode of the first APV in peak mode, (d) the cluster charge distribution in peak mode for each optical channel, (e) normalized distributions of the signal-to-noise ratio for peak (green/light grey) and deconvolution mode (black), (f) ENC in peak mode, (g) bias voltage scan.
All measurements were made in the cold environment.
The peak of clusters with low S/N in deconvolution mode in (e) is due to particles from the previous bunch crossing of the LHC-like pion beam that are sampled at their tail.

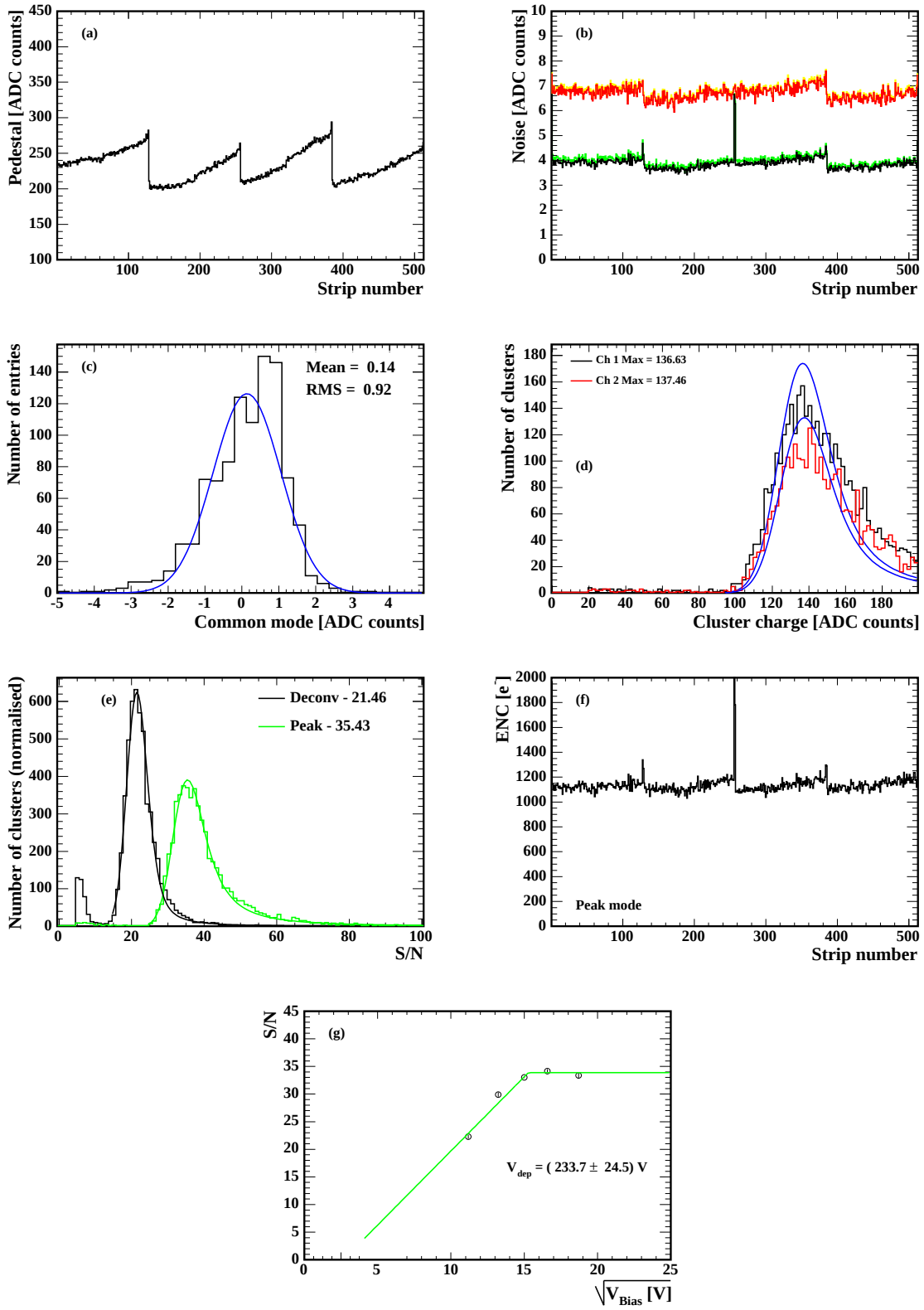

Figure 42: Characteristic distributions for a ring 7 module (module 7.3) on the front petal: (a) pedestal distribution, (b) raw and common mode subtracted noise for peak (green and black curves) and deconvolution mode (yellow and red curves), (c) common mode of the first APV in peak mode, (d) the cluster charge distribution in peak mode for each optical channel, (e) normalized distributions of the signal-to-noise ratio for peak (green/light grey) and deconvolution mode (black), (f) ENC in peak mode, (g) bias voltage scan.
All measurements were made in the cold environment.
The peak of clusters with low S/N in deconvolution mode in (e) is due to particles from the previous bunch crossing of the LHC-like pion beam that are sampled at their tail.

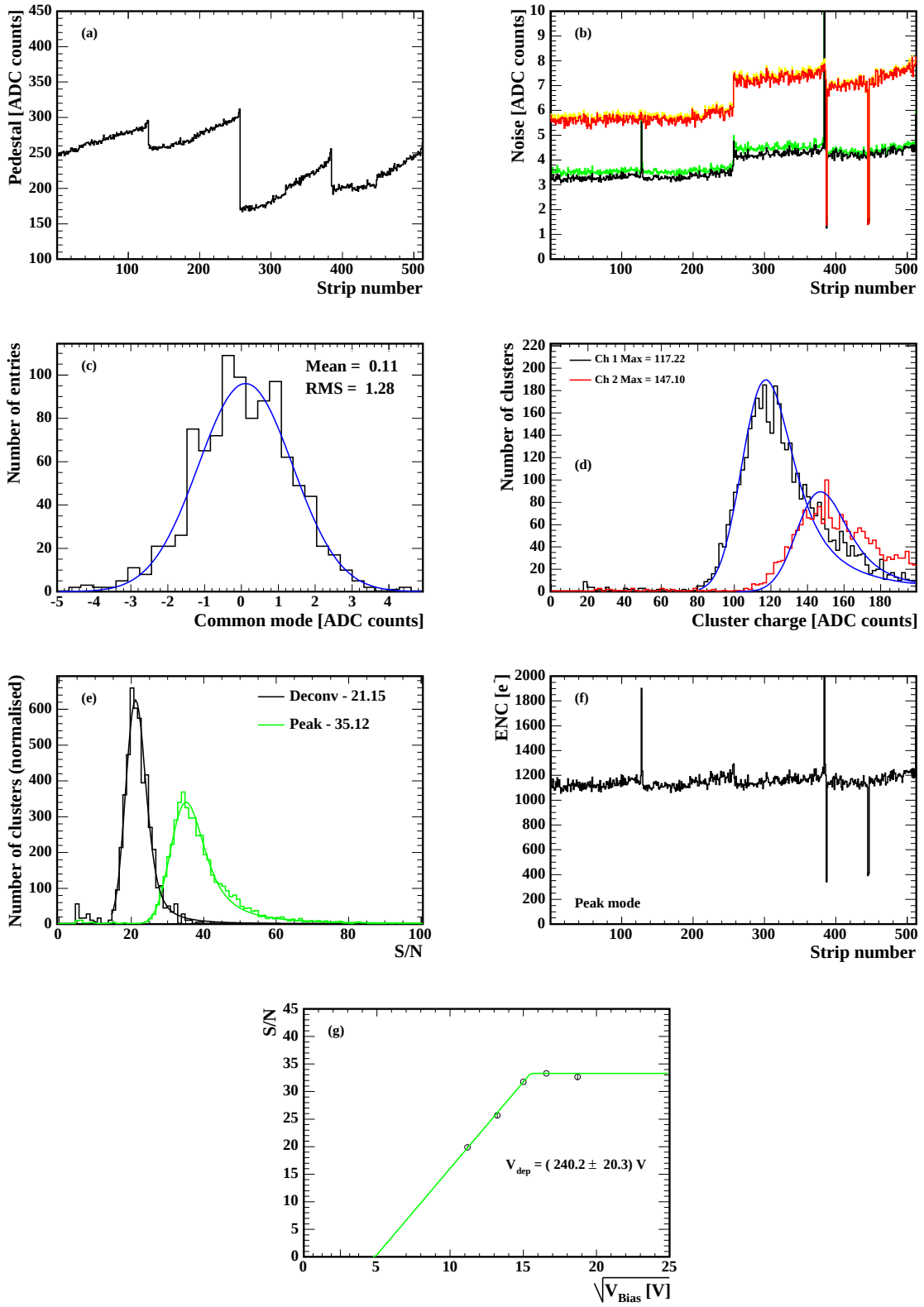

Figure 43: Characteristic distributions for a ring 7 module (module 7.2) on the back petal: (a) pedestal distribution, (b) raw and common mode subtracted noise for peak (green and black curves) and deconvolution mode (yellow and red curves), (c) common mode of the first APV in peak mode, (d) the cluster charge distribution in peak mode for each optical channel, (e) normalized distributions of the signal-to-noise ratio for peak (green/light grey) and deconvolution mode (black), (f) ENC in peak mode, (g) bias voltage scan.
All measurements were made in the cold environment.